# Unequal socioeconomic exposure to drought extremes induced by stratospheric aerosol injection Weijie Fu<sup>1</sup>, Xu Yue<sup>1, \*</sup>, Chenguang Tian<sup>1</sup>, Rongbin Xu<sup>2</sup>, Yuming Guo<sup>2</sup> <sup>1</sup> State Key Laboratory of Climate System Prediction and Risk Management, Jiangsu Collaborative Innovation Center of Atmospheric Environment and Equipment Technology, School of Environmental Science and Engineering, Nanjing University of Information Science & Technology (NUIST), Nanjing, 210044, China <sup>2</sup> Climate, Air Quality Research Unit, School of Public Health and Preventive Medicine, Monash University, Melbourne, Australia. \*Correspondence to: Xu Yue, yuexu@nuist.edu.cn

#### **Abstract**

18

19

20

21

22

23

24

25

26

27

28

29

30

31

32

33

34

35

36

37

38

39

40

As global temperature rises, the severity and frequency of droughts are projected to increase. Stratospheric aerosol injection (SAI) has been proposed as a potential solution to reduce surface temperatures, but its effectiveness in alleviating drought extremes remains unclear. Here, we assess the global impacts of SAI on drought extremes based on experiments from the Geoengineering Model Intercomparison Project phase 6 (GeoMIP6) and the Geoengineering Large Ensemble Project (GLENS). By 2100, the frequency of extreme droughts is projected to increase by 7.33% under the highemission Shared Socioeconomic Pathways 5 (SSP5-8.5) scenario relative to present day. SAI reduces this increase by 1.99% in GeoMIP6, and by 1.80% in GLENS compared with Representative Concentration Pathways 8.5 (RCP8.5). Attribution analyses show that SAI-induced cooling alone reduces extreme drought frequency by 3.42% in GeoMIP6 and 4.28% in GLENS relative to their respective high-emission scenarios, outweighing the 2.12% increase driven by SAI-induced precipitation reductions under the same conditions. However, these rainfall deficits lead to substantial inequities in drought exposures. Compared to developed nations, countries with less development experience smaller reductions, or even increases, in economic and population exposure to extreme drought under SAI relative to SSP5-8.5 or RCP8.5. These findings suggest that the current SAI strategies in GeoMIP6 and GLENS may induce the risk of unintentionally worsening regional hydroclimatic disparities.

#### 1 Introduction

41

42 Global warming is profoundly shaping the Earth with reduced sea ice (Diffenbaugh 43 et al., 2013), raised sea level (Tebaldi et al., 2021), and increased climatic extremes 44 (Song et al., 2022). Persistent warming has expanded the land area with decreased 45 precipitation but increased evaporation, enhancing the frequency and severity of global drought events (Dai, 2011a; Trenberth et al., 2014; Samaniego et al., 2018). As one of 46 47 the most destructive and persistently widespread natural disasters, drought can have significant impacts on human survival, the economy, and societal structures (Dai, 2013; 48 49 Carrão et al., 2016; Yue et al., 2021). During 1970-2019, droughts were responsible for 50 34% of disaster-related fatalities(Smith, 2021) and annually erode 12 million hectares of arable land (Diallo, 2008), leading to reduced agricultural yields, increased food 51 52 prices, and escalated economic instability especially for vulnerable populations (Rusca et al., 2023). 53 Mitigating global warming requires reducing anthropogenic GHG emissions. 54 55 However, due to the inertia of climate system, global temperature responses lag behind 56 emission reductions. Geoengineering, particularly Solar Radiation Management (SRM), 57 has been proposed as a potential climate change mitigation approach (Ricke et al., 2012). 58 The SRM aims to reflect incoming solar radiation back into space (Irvine et al., 2012), 59 reducing global surface temperatures (Irvine et al., 2019; Duffey and Irvine, 2024). As one type of SRM, stratospheric aerosol injection (SAI) has gained significant attentions 60 61 due to its cost-effectiveness and practicality (Smith and Wagner, 2018; Smith, 2020). 62 This method introduces reflective aerosols into the stratosphere to increase the Earth's 63 albedo (Pope et al., 2012), mimicking the cooling effects observed after volcanic 64 eruptions (Wilson et al., 1993). 65 Earth System Models (ESMs) are vital for analyzing climatic impacts and the 66 potential side effect of SRM before its implementation (Macmartin and Kravitz, 2019). 67 The Geoengineering Model Intercomparison Project phase 6 (GeoMIP6) (Kravitz et al., 2011; Visioni et al., 2023) was established to assess climatic responses to 68 69 geoengineering using multiple ESMs under various forcing scenarios. In contrast, the 70 Geoengineering Large Ensemble (GLENS) project performed multiple experiments 71 with a single ESM, exploring different injection strategies (Tilmes et al., 2018). 72 Ensemble of these simulations indicated that SAI could alter global hydrological cycle 73 relative to high emission scenario (Jiang et al., 2024; Rezaei et al., 2025). Notably, the

magnitude and spatial pattern of rainfall changes exhibit strong dependence on injection latitudes and altitude (Zhao et al., 2021; Krishnamohan and Bala, 2022). Region-specific analyses suggest that specific SAI deployment strategies may mitigate extreme drought risks under the Shared Socioeconomic Pathways 5 (SSP5-8.5) scenario. For instance, in Cape Town, South Africa, model ensembles indicate a potential 90% reduction in extreme drought risk when applying the GLENS injection protocol (Botai et al., 2017; Odoulami et al., 2020). However, these benefits are highly contingent upon the specific implementation strategy: different SAI designs or distinct greenhouse gas background conditions (e.g., SSP2-4.5) could result in neutral or adverse outcomes (Du et al., 2025). Nevertheless, the benefits of SAI on reducing drought extremes remain unclear on the global scale.

In this study, we use ensemble simulations from both GeoMIP6 and GLENS to assess 1) how SRM strategies alter the magnitude and spatial distribution of extreme drought risk under high-emission scenarios, and the climatic mechanisms that govern these changes; and 2) how the magnitude of SRM-derived drought exposure reduction varies across countries with different levels of socioeconomic development. For GeoMIP6, we consider two types of SRM including G6solar by reducing solar constant and G6sulfur by SAI. We employ the self-calibrating Palmer Drought Severity Index (scPDSI) to quantify drought levels, due to its ability to depict drought state through dynamically calculated climatic thresholds adapted to regional environment (Wells et al., 2004; Dai, 2011b). We quantify changes in the probability of extreme drought with and without SRM interventions under high-warming scenarios (SSP5-8.5 for GeoMIP6 and RCP8.5 for GLENS), both of which assume strong warming with radiative forcing reaching 8.5 W m<sup>-2</sup> by the end of this century. We explore uncertainties associated with different SAI strategies, including the fixed equatorial injection approach adopted in G6sulfur (GeoMIP6) and the multi-latitude aerosol placement used in GLENS. We pay special attentions to the possible disparity of extreme drought responses to the SAI among countries with different socioeconomic development.

### 2 Method

# 2.1 Model data

We use outputs from multiple models participating in the G6solar and G6sulfur experiments of GeoMIP6 (Table 1). The G6sulfur experiment involves the injection of

sulfur dioxide (SO<sub>2</sub>) within the 10°S-10°N latitude band along the 0° longitude at altitudes of 18–20 km from the year 2020. The SO<sub>2</sub> injection rate is adjusted annually or every decade to lower the global mean surface air temperature from the high forcing scenario (SSP5-8.5) to the medium forcing scenario (SSP2-4.5) (Kravitz et al., 2015). This scheme aims to achieve a more uniform global distribution of sulfate aerosols compared to the single-point injections (English et al., 2012). For some models, prescribed sulfate distribution in stratosphere is applied. As a comparison, G6solar experiment directly reduces the solar constant in an idealized manner to achieve the same reduction in radiative forcing from the high to medium scenario (Kravitz et al., 2015). We use historical simulations and future projections under the SSP5-8.5 scenario to assess the mitigating effects of different SRMs. Some models provide multiple realizations for both historical and SSP5-8.5 experiments. We analyze data only from ensemble members that have the same realizations in both the G6sulfur and G6solar experiments. As a result, we select five available climate models participating in the GeoMIP6 experiment (Table 1) with qualified outputs to calculate changes in drought state from the present day to the end of the 21st century. All model data with varied spatial resolutions are interpolated to the same grid of 1°×1° to facilitate the calculation of multi-model ensemble mean. Inter-model consistency was evaluated based on the number of models that aligned with the direction of the multi-model ensemble change. Changes in the multi-model ensemble were deemed robust if more than four models exhibited changes with the same sign; otherwise, these changes were considered uncertain.

107

108

109

110

111

112

113

114

115

116

117

118

119

120

121

122

123

124

125

126

127

128

129

130

131

132

133

134

135

136

137

138

139

To evaluate the robustness of our findings, we conducted a comparative analysis with the Geoengineering Large Ensemble Project (GLENS) (Tilmes et al., 2018). Unlike the idealized equatorial injection strategy employed in G6sulfur, GLENS implements a feedback-control algorithm designed to maintain global mean surface temperature, interhemispheric temperature gradients, and equator-to-pole temperature gradients at 2020 levels under a high-emission RCP8.5 scenario (Kravitz et al., 2017). This approach injects sulfate aerosols at four locations along 180° longitude (15°N, 15°S, 30°N, and 30°S) at latitudinally optimized altitudes. Based on predefined temperature targets, the sulfate aerosol injection rate is dynamically adjusted at each location. The GLENS dataset consists of a 20-member ensemble generated by the NCAR Community Earth System Model (CESM1), which incorporates the Whole

Atmosphere Community Climate Model (WACCM) as its atmospheric component (Table 2). Our analysis exclusively considered ensemble members with continuous simulations spanning the entire 21<sup>st</sup> century across both feedback and control experiments (001, 002, and 003). This comparative framework allows us to assess the sensitivity of drought extremes and socioeconomic exposure to different SAI deployment strategies.

# 2.2 Socioeconomic data and exposure

We use Gross Domestic Product (GDP) data (Geiger, 2018) with a spatial resolution of 0.25° from 2000 to 2020, along with GDP projections for 2025-2100 under the SSP5-8.5 scenario (Dellink et al., 2017). The GDP values are standardized to the 2005 purchasing power parity (PPP) international dollar for comparability (Geiger, 2018; Wang and Sun, 2022). Population data at 1-km resolution, including urban, rural, and total populations, are sourced from the Socioeconomic Data and Applications Center (SEDAC) for five-year intervals from 2000 to 2020 (Jones and O'neill, 2020). For future projections, we use population data at ten-year intervals and one-eighth degree resolution in space under the SSP5-8.5 scenario for 2020-2100 (Jones and O'neill, 2016, 2020). The GDP (or population) exposure is calculated as the frequency of extreme drought multiplied by the GDP (or population) values in each grid cell (Sun et al., 2022).

The Human Development Index (HDI) from the Human Development Report is used to differentiate the economic development of various countries and regions (Undp, 2024). In total, 158 countries with land area larger than 10000 km² (the size of at least one 1°×1° grid) are selected and separated into four HDI groups including low (HDI<0.55), medium (0.55<HDI<0.699), high (0.7<HDI<0.799), and very high (HDI>0.8) levels following the suggested criteria (Undp, 2024). The gridded GDP or population exposure is summed up for each country, and then aggregated into four HDI groups accordingly.

# 2.3 Drought indices

We use scPDSI as the primary metric to quantify the spatiotemporal variations of drought events. The scPDSI is calculated separately for each model with the corresponding meteorological variables. At each grid, monthly precipitation (P),

173 potential evapotranspiration (PET) and the available water holding capacity (AWC) are used to assess drought severity based on dynamically computed thresholds from 174 175 historical reference period climates (Wells et al., 2004). There are two common 176 methods for calculating PET: the Penman-Monteith and Thornthwaite parameterization schemes (Penman and Keen, 1948; Thornthwaite, 1948; Monteith, 1965). In this study, 177 178 we use the Penman-Monteith equation, which calculates PET base on surface air temperature  $(T, {}^{\circ}C)$ , net surface radiation  $(Rn, MJ day^{-1} m^{-2})$ , surface specific humidity 179 180 (q, kg/kg), two-meter wind speed (U, m/s), and surface air pressure (p, kPa):

181 
$$PET_{pm} = \frac{\Delta \cdot Rn + 6.43\gamma(1 + 0, .536U)(e_s - e_a)}{(\Delta + \gamma)\lambda}$$
 (1)

where  $\Delta$  is the slope of the saturation vapor pressure curve,  $\gamma$  is psychrometric 182 coefficient,  $\lambda$  is latent heat of vaporization,  $(e_s - e_a)$  is the saturation vapor pressure 183 deficit, which can be calculated by air temperature, specific humidity, and air pressure 184 185 at the surface:

186 
$$e_s - e_a = 0.6112e^{\left(\frac{17.62T}{243.12+T}\right)} - \frac{p \cdot q}{q + 0.622(1-q)}$$
 (2)

Since CMIP6 provides wind speeds at 10 meters above the surface, we convert them to 187 wind speed at 2 meters (Allan et al., 1998): 188

189 
$$U_2 = \frac{4.87}{\ln(67.8 * z - 5.42)} U_{10} \tag{3}$$

191

Here z = 10 meters. The calculation of PDSI requires the use of P, PET, and AWC to 190 calculate eight variables related to soil moisture based on the water balance: 192 evapotranspiration (ET), recharge (R), runoff (RO), loss (L), potential 193 evapotranspiration (PE), potential recharge (PR), potential runoff (PRO), and potential 194 loss (PL) (Webb et al., 2000). These variables are then used to calculate the Climatically 195 Appropriate For Existing Conditions' (CAFEC) precipitation  $(\hat{P})$ :

$$\hat{P} = \alpha P E + \beta P R + \gamma P R O - \delta P L \tag{4}$$

Here,  $\alpha$ ,  $\beta$ ,  $\gamma$  and  $\delta$  are the water-balance coefficients, which are derived from ET, R, 197 198 RO, and L divided by their potential values, respectively. The difference between P and  $\hat{P}$  is defined as moisture departure (d): 199

$$200 d = P - \hat{P} (5)$$

201 The d is scaled to a moisture anomaly index (Z index) using climatic characteristic (K):

$$Z = dK (6)$$

203 K can be calculated by potential evapotranspiration, recharge, runoff, precipitation, loss 204 and moisture departure:

205 
$$K_{i}' = 1.5 \log_{10} \left( \frac{\frac{\overline{PE_{i}} + \overline{R_{i}} + \overline{RO_{i}}}{\overline{P_{i}} + \overline{L_{i}}} + 2.8}{\overline{D_{i}}} \right) + 0.5$$
 (7)

$$K_{i} = \frac{17.67}{\sum_{j}^{12} \bar{D}_{j} K_{j}'} K_{i}'$$
 (8)

- Where  $\overline{D}$  is the average monthly moisture departure, 17.67 is an empirical constant.
- 208 The PDSI for a given month is calculated using the Z index and empirical parameters:

$$PDSI_{i} = 0.897PDSI_{i-1} + \left(\frac{1}{3}\right)Z_{i} \tag{9}$$

The duration factors (0.897 and 1/3) are empirical parameters obtained by Palmer from previous studies (Alley, 1984). The original drought index, PDSI, is calculated using fixed climatic thresholds that are not comparable across different climatic regions. To address such limitation, the scPDSI employs dynamic climatic characteristic and duration factors based on the regional environment, offering the advantage of both spatial and temporal comparability (Wells et al., 2004; Dai, 2011b; Van Der Schrier et al., 2013). In the calibration of PDSI, monthly K was adjusted using local climate statistics to ensure that extreme drought events (PDSI  $\leq$  -4.0) and wet periods (PDSI  $\geq$  4.0) occur at frequencies of approximately 2%. The duration factors were derived from linear regression analyses of accumulated Z-index values during extreme drought and wet conditions, thereby enhancing sensitivity to regional climate variability.

The standard scPDSI values range from -4 to 4, representing conditions from extremely dry to extremely wet. In this study, an extreme drought month is defined if scPDSI value is lower than -4. The frequency of drought extremes for a given scenario is calculated as the fraction of extreme drought months out of a 240-month period. The absolute changes of such frequency are compared among scenarios and SAI strategies. Additionally, we compute other drought indices for comparisons, including the PDSI, Palmer Modified Drought Index (PMDI), Palmer Hydrological Drought Index (PHDI), and Palmer Z Index (Z-index).

### 2.4 Mitigation Potential (MP)

We define the MP value to quantify the extent to which SRM could mitigate the increased drought risks induced by climate warming:

$$MP = \frac{P_{SRM} - P_{SSP585}}{P_{SSP585} - P_{hist}} \tag{10}$$

Here,  $P_{hist}$  represents the drought probability or the exposure (either GDP or population) 234 to drought extremes (scPDSI < -4) at present day averaged for the period of 1995-2014. 235 236  $P_{SSP585}$  and  $P_{SRM}$  represent the mean drought probability/exposure at 2081-2100 under 237 the SSP5-8.5 and SRM (G6solar or G6sulfur) scenarios, respectively. We calculate the 238 MP values for four different HDI groups of countries by summing the GDP or 239 population exposure within each HDI group. For individual countries, we calculate the 240 MP values based on the GDP or population exposure for that specific country. Our 241 analyses showed that the denominator of Equation (10) is positive for all four HDI 242 groups and for 96% of the 158 countries, indicating that extreme drought exposure is 243 projected to increases in the future under the SSP5-8.5 scenario. A negative MP value 244 indicates that SRM helps mitigate the warming-induced increase of extreme drought exposure, and vice versa. The units of the MP value can be expressed as a percentage 245 246 (when MP<1) or as a ratio (when MP>1).

247248

### 2.5 Drought Exposure Disparity (DED)

The DED values are defined to assess the disparity of extreme drought exposure among countries with different HDI:

$$DED = \frac{P_{low \, HDI}}{P_{very \, high \, HDI} + P_{high \, HDI}} \tag{11}$$

Here,  $P_{low\ HDI}$  represents the sum of the exposure (GDP or population) to drought extremes (scPDSI < -4) for all low HDI countries.  $P_{very\ high\ HDI}$  and  $P_{high\ HDI}$  are exposures in very high HDI countries and high HDI countries, respectively. An increase of DED indicates an enhanced inequality for the socioeconomic exposure to drought extremes.

257258

259

260

261

262

252

253

254

255

256

#### 2.6 Calculations and attributions of scPDSI

For each climate model of GeoMIP6, we collect monthly temperature, precipitation, and radiation to calculate historical scPDSI using present-day climatic variables and future scPDSI using meteorology from the SSP5-8.5, G6sulfur, or G6solar scenarios (Table 3). To identify the main drivers of scPDSI changes, we perform 9 additional

sensitivity offline experiments by combining historical meteorological forcings with future projections (Table 3). In these offline experiments, we replace one variable at a time from the SSP5-8.5 scenario with the corresponding future projections from GeoMIP6 scenarios. The differences in scPDSI between sensitivity experiments and the full sets of future projections (SSP5-8.5 or GeoMIP6) indicate the relative impact of individual climatic forcing on changes in scPDSI. We select 1995-2014 as the historical reference period and 2081-2100 as the future projection period for analyses. Similarly, we conducted offline calculations of scPDSI for the GLENS and RCP8.5 scenarios.

272273

274

275

276

277

278

279

280

281

282

283

284

285

286

287

288

289

290

263

264

265

266

267

268

269

270

271

#### 2.7 Model evaluations

Monthly precipitation and temperature from the CRU TS (Climate Research Unit Gridded Time Series) dataset version 4.07 are used to evaluate the model's performance in reproducing present-day climate (Harris et al., 2020). Both the CRU data and model output are interpolated to  $1^{\circ} \times 1^{\circ}$ . We calculate the correlation coefficient (R, 1 is best), standard deviation ratio (SDEV, 1 is best), and centered root-mean-square error (CRMSE, 0 is best) between the CRU data and model simulations (Taylor, 2001). For temperature, all models reproduce the observed spatial pattern with R>0.98 and SDEV ranging from 0.95 to 1.08 (Fig. 1a). The CRMSE for most models is less than 2, except for IPSL-CM6A-LR (2.24). For precipitation, R ranges from 0.74 to 0.85, SDEV ranges from 0.82 to 1, and CRMSE ranges from 0.99 to 1.55 (Fig. 1b). Although the R for simulated precipitation is lower than that for temperature, the CRMSE is generally lower. Overall, the selected models reasonably reproduce the observed meteorology with low biases. While all models accurately capture the changing characteristics of temperature and precipitation, differences in parameterization schemes for radiation, cloud-aerosol interactions, aerosol microphysics, and other factors result in variations in the simulated patterns of meteorological factors (Mauritsen et al., 2019; Visioni et al., 2021). Therefore, we use the multi-model ensemble to minimize biases caused by inter-model variations.

291292

293

294

### 3 Results

# 3.1 Responses of temperature and precipitation to SRM

By the end of 21<sup>st</sup> century, global land surface air temperature is projected to increase by 5.73°C under the SSP5-8.5 scenario relative to 1995–2014 (Fig. 2a). Such warming is more significant at the mid-to-high latitudes in Northern Hemisphere (NH). The pronounced temperature rise intensifies hydrological cycle, evidenced by enhanced water vapor content in lower troposphere (Held and Soden, 2006), resulting in an increased global average precipitation of 0.18 mm/day (Fig. 2d). However, a discernible reduction of rainfall is noted in regions including northern South America, southern Africa, Australia, southern North America, and western Europe.

Reduction of the solar constant in G6solar causes an intense cooling worldwide (Fig. 2b), resulting in a decrease in global average land surface air temperature of approximately -2.61°C and counteracting 45.6% of the warming in SSP5-8.5. For G6sulfur, the injection of sulfur aerosols (or SO<sub>2</sub>) contributes to a reduction in global average surface temperature of about -2.45°C, offsetting 42.8% of the SSP5-8.5 warming (Fig. 2c). Although both SRMs mitigate less than half of the temperature rise, they offset most of the increase in precipitation attributable to global warming (Figs 2e and 2f) (Niemeier et al., 2013; Ricke et al., 2023). The SRM-induced tropospheric cooling weakens tropical circulation, inhibiting convection and subsequently reducing precipitation (Ferraro et al., 2014). This reduction in temperature and precipitation is more pronounced in the GLENS simulations (Fig. 3). By the end of this century, the GLENS strategy successfully maintained the temperature at 2020 level, reducing the global average by 5.48°C compared to the RCP8.5 scenario. Due to the different injection magnitude and locations from GeoMIP6, the GLENS injection results in more pronounced precipitation reduction in central Africa, India, and high-latitude regions of the NH (Fig. 3d).

# 3.2 Responses of drought extremes to SRM

Following the intense warming, frequency of extreme drought events increases by 7.33% globally at 2081-2100 under the SSP5-8.5 scenario compared to the present period (Fig. 4a). Such an enhancement is more pronounced at the mid-to-high latitudes, especially in the Southern Hemisphere (SH, e.g., Australia and southern Africa) where precipitation is projected to decrease (Fig. 2d). In contrast, the wet tendencies in some tropical areas (e.g., India and central Africa) and boreal regions outweigh the local

warming, resulting in alleviated drought stresses at the low or high latitudes of both hemispheres.

The SRM shows good potentials to decrease extreme drought occurrences. Compared to SSP5-8.5, G6solar reduces the frequency of extreme drought events by 2.12% globally at 2081-2100 (Fig. 4d), mitigating 28.9% of the SSP5-8.5-induced drought stress increment. Regionally, drought extremes are projected to decline uniformly at most latitudes, with stronger amelioration over Europe, Australia, and southern Africa where precipitation increases by G6solar (Fig. 2e). With G6sulfur, a similar reduction of 1.99% (MP=27.1%) is predicted for global drought extremes but with large spatial heterogeneity (Fig. 4g). Most of such reductions are located in the SH, especially over Australia and southern Africa. In contrast, the frequency of drought extremes enhances significantly in central Africa, following the G6sulfur-induced precipitation deficit (Fig. 2f). This region has been enduring prolonged droughts since the 1990s, demonstrating high vulnerability to climate change impacts (Zhou et al., 2014; Kendon et al., 2019; Palmer et al., 2023).

The SAI in GLENS exhibits stronger MP than G6sulfur in reducing the frequency of extreme droughts. Compared to the present day, the global drought probability increases by 1.92% during 2075-2094 under the RCP8.5 scenario (Fig. 5a). This increment is smaller than the 7.33% projected under SSP5-8.5 (Fig. 4a), because RCP8.5 produces a larger rise in global precipitation (Fig. 3c) than SSP5-8.5 (Fig. 2d). Relative to RCP8.5, SAI in GLENS reduces the global frequency of extreme droughts by 1.8% (Fig. 5b), offsetting nearly all of the drought increase caused by RCP8.5 warming (MP=93.8%). Compared to G6sulfur, GLENS shows enhanced MP over northern Eurasia, South America, and North America. This may be attributed to its multi-latitude injection strategy and the dynamic adjustment of injection amounts at different latitudes to fully offset future warming (Fig. 3). In contrast, significant drought amplification is projected with GLENS in India, northern Asia, and Alaska relative to RCP8.5 (Fig. 5b), a pattern not seen under G6sulfur (Fig. 4g).

# 3.3 Attribution of extreme drought response to SRM

We performed sensitivity experiments to quantify the contributions of changes in temperature, precipitation, and radiation to the variations of extreme droughts. By the end of the century, changes in temperature and radiation under the SSP5-8.5 scenario

lead to an increased frequency of extreme drought events compared to the historical period (Fig. 4b). Significant warming alone (Fig. 2a) enhances the frequency of extreme droughts globally by 5.43% (Fig. 6a), with the most pronounced increases in the midand high-latitudes of the NH. Meanwhile, net radiation increases by 5.28 W m<sup>-2</sup>, thus intensifying PET and worsening drought frequency by 1.05% (Fig. 6g). In contrast, the increase in global precipitation (Fig. 2d) under SSP5-8.5 reduces the frequency of drought extremes by 2.12% globally and across most regions, except for southern Africa, Australia, and western Europe (Fig. 6d). On the global scale, warming is the dominant factor driving changes in drought extremes over 50.17% of land area (excluding ice and desert), surpassing the 47.97% influenced by precipitation (Fig. 4c). Relative to SSP5-8.5, SRM-induced cooling alone reduces extreme drought frequency by 3.44% in G6solar (Fig. 4e) and 3.42% in G6sulfur (Fig. 4h). This mitigation shows a very similar spatial pattern between the two SRMs, with a more pronounced effect at mid-high latitudes in the NH (Figs 6b and 6c). Additionally, the reduction of solar radiation due to dimming effects further alleviates global drought extremes by 0.85% for G6solar (Fig. 6h) and 1.42% for G6sulfur (Fig. 6i). However, SRM-induced rainfall deficits (Figs 2e and 2f) increase the frequency of extreme drought by 1.61% for G6solar (Fig. 6e) and 2.12% for G6surfur (Fig. 6f) relative to SSP5-8.5 scenario, with the most significant impacts occurring in central Africa where the reduction in precipitation is at its maximum. These changes partly offset the cooling-induced mitigation, resulting in patchy responses of drought extremes in the NH (Figs 4d and 4g). Compared to G6solar, the rainfall deficit is larger in G6sulfur, leading to an enhanced frequency of drought extremes in central Africa, the eastern U.S., and eastern Europe. Consequently, changes in precipitation act as the dominant driver of extreme drought over 48.0% land areas in G6sulfur (Fig. 4i), larger than that of 39.9% in G6solar (Fig. 4f). Compared with RCP8.5, the SAI-induced cooling in GLENS reduces the frequency of extreme droughts by 4.28% by the end of the century (Fig. 7a). In contrast, the precipitation reduction in GLENS increases global extreme drought frequency by 2.12% (Fig. 7b), with regional hotspots in central Africa, India, North America, and northern Asia, consistent with the spatial pattern of the SAI-induced rainfall deficit (Fig. 3d). These patterns resemble those in G6sulfur (Figs 6c and 6f), except that the cooling-

360

361

362

363

364

365

366

367

368

369

370

371

372

373

374

375

376

377

378

379

380

381

382

383

384

385

386

387

388

389

390

391

392

induced drought reduction is larger in GLENS, due to its stronger cooling effect (Fig.

3b vs. Fig. 2c). Overall, SAI-induced cooling plays the dominant role in mitigating the projected increase in extreme drought frequency under a warming climate, although the level of alleviation may vary across SAI strategies because of differences in injection locations and sulfate amounts.

### 3.4 Global socioeconomic disparity in exposure to drought extremes

To quantify socioeconomic exposure to drought extremes under future warming and SRM scenarios, we analyzed variations of global GDP and population exposure to drought extremes across different scenarios. Compared to present day, there are significant increases of \$72.1 trillion in GDP and 460 million in population exposed to extreme drought every year by the end of century under the SSP5-8.5 scenario (Figs 8a and 8d). High exposure areas are located in eastern North America, western Europe, and eastern China. As an effective mitigation, G6solar can reduce annual GDP exposure by \$18.6 trillion and population exposure by 142 million people to extreme drought (Figs 8b and 8e), resulting in the MP of -25.8% for GDP and -30.9% for population. As a comparison, the MP of G6sulfur is lower at -17.9% for GDP and -22.5% for population (Figs 8c and 8f). The SAI in GLENS achieves a similar global MP of -19.6% in GDP to that in G6sulfur (Fig. 9b). However, it results in a 15.9% increase in global population exposure to extreme drought relative to SSP5-8.5, mainly because of the substantial enhancement of drought risks in India, central Africa, and eastern China (Fig. 9d).

The spatial heterogeneity of these mitigations results in pronounced disparities among countries at different development levels, as measured by HDI. G6solar reduces GDP exposure to drought extremes by 35.1% in very high HDI countries and by 19.9% in high HDI countries, but only 11.2% in countries with low HDI (Fig. 10a). This disparity becomes even more pronounced under the G6sulfur scenario, in which the frequency of GDP exposure to drought extremes instead increases by 12.6% relative to SSP5-8.5 for low HDI countries, with the highest risks in South Sudan, Rwanda, and Burundi (Fig. 10e). It is important to note that under both SRMs, the exposure of the GDP and population for the low HDI countries varies to a certain extent among models. However, most models project elevated risks, suggesting that these nations may remain highly vulnerable. Both SRMs result in relatively weaker MP for population exposure compared to GDP in low and medium HDI countries, with G6sulfur even increasing

population exposure by up to 42.9% in low HDI countries. Similar to GDP, the top 5 countries suffering the largest increases in population exposure are located in central Africa (Fig. 10f). As a comparison, the SAI in GLENS shows pronounced risk amplification, with notably elevated drought exposure for medium- and low-HDI countries compared to the SRM approaches in GeoMIP6 (Figs 10a-b).

We use the index of drought exposure disparity (DED) to indicate the inequity of drought exposure between high- and low-HDI countries. Compared to SSP5-8.5, G6solar increases the DED of GDP by 12.72% and that of population by 30.58%. Under G6sulfur, this disparity is even more pronounced, with DED values increasing by 22.74% for GDP and 36.34% for population, with GLENS experiment increasing 244.37% for GDP and 251.18% for population.

### 4 Discussion and conclusions

Global warming is projected to enhance future drought risks (Dai, 2013). SRM is hypothesized to partially offset warming, but its regional climatic and societal impacts remain uncertain (Irvine et al., 2019). Our analyses show asymmetric responses in temperature and precipitation to SRM. For example, the SAI in G6sulfur mitigates only 42.8% of the SSP5-8.5 warming (Fig. 2c) but offsets 88.9% of the rainfall increase under SSP5-8.5 (Fig. 2f), indicating a disproportionate suppression of the water cycle. While cooling directly reduces evaporation, aerosol-induced increase in atmospheric stability indirectly weakens monsoon circulation (Tilmes et al., 2013; Krishnamohan and Bala, 2022), such as India and China (Fig 2e). Consequently, SRM may inadvertently degrade hydroclimate security in vulnerable regions under a high-emission scenario.

Relative to G6solar, precipitation is even more inhibited in G6sulfur especially over central Africa (Fig. 2f), because the absorbing sulfate aerosols induces an anomalous stratospheric heating that further enhances air stability (Simpson et al., 2019; Tilmes et al., 2022). In addition, under the GLENS scenario, SAI overcompensates for the greenhouse gas-forced expansion of the Hadley Circulation (Cheng et al., 2022) and offsets the poleward shift of storm tracks in the mid-latitude of NH (Karami et al., 2020). These changes, along with a more positive phase of the North Atlantic Oscillation induced by SAI (Jones et al., 2022), resulting in increased exposures to drought in Europe and the northeastern U.S. (Figs 4d and 4g).

Previous studies have revealed the negative impacts of SAI on hydrological cycles, but they mainly highlighted the benefits of SAI in mitigating temperature and precipitation extremes induced by climate warming (Jones et al., 2017; Irvine et al., 2019). However, variations of drought involve complex relationships between temperature and precipitation, leading to nonlinear responses of drought to the perturbations in these climatic variables. For instance, the sum of the contributions of individual climatic factors is not fully equal to the total changes in drought extremes under the SSP5-8.5 and two SRM scenarios (Figs 4 and 6).

Few studies have explored the SAI impacts on global drought using specific drought indices (Abiodun et al., 2021; Liu et al., 2024), but they tend to focus on the mean state of drought events rather than drought extremes. Our additional analyses showed very limited changes in the mean scPDSI values for both G6solar and G6sulfur relative to the SSP5-8.5 scenario on the global scale (Figs 11a-11c). The regional reduction (indicating a drier state) of scPDSI by G6sulfur is also smaller in magnitude than the increase (indicating a wetter state) under SSP5-8.5 over central Africa, masking the unbalanced responses as shown for the drought extremes (Fig. 4).

The climatic effects of SAI vary depending on the intensity and deployment strategies. Under the same high-emission scenario, the SAI in GeoMIP6 (G6sulfur) experiment aims to limit global warming to a moderate level, whereas GLENS implements SAI intensively to maintain the temperature at the level of 2020 (Tilmes et al., 2015; Tilmes et al., 2018). Furthermore, these two experiments employ distinct injection methodologies, with the multi-latitude aerosol deployment in GLENS but fixed equatorial injection in G6sulfur. Despite these differences, both GLENS and G6sulfur exhibit similar spatial patterns in their impacts on extreme drought (Figs 4g and 5b). However, regional differences, particularly in India and northern China, lead to different levels of extreme drought risk for the global economy and population.

Our findings are subject to some limitations and uncertainties. First, differences in model configurations may affect the predicted impacts of SRM. For instance, the IPSL-CM6A-LR and UKESM1-0-LL models simulate changes in stratospheric chemistry by using actual injected SO<sub>2</sub>, whereas CNRM-ESM2-1 and MPI-ESM1.2 employ prescribed distributions of stratospheric aerosol (Tilmes et al., 2015; Niemeier et al., 2020; Visioni et al., 2021). Although each model predicts comparable cooling effects, variations in the SAI implementation may lead to discrepancies in precipitation

perturbations that are vital for predicting drought responses. Here, we employed a multi-model ensemble to derive climatic changes that are consistent among the majority of models. Second, the application of a single drought index may influence the projection results. For this study, we used scPDSI due to its clear physical meaning, adaptive climatic responses, and specific criteria for drought extremes (Wells et al., 2004). As a comparison, we checked other drought indices such as PDSI, Palmer Modified Drought Index (PMDI), Palmer Hydrological Drought Index (PHDI), and Palmer Z Index (Z-index). Projections using these indices showed similar patterns to scPDSI though with spatially varied magnitude (Fig. 11), suggesting that our main conclusions are not affected by the selection of the drought index. Third, uncertainties in future projections of GDP and population may affect exposure to drought extremes. In this study, we applied the future estimates of GDP and population density from the SSP5-8.5 scenario by the end of the 21<sup>st</sup> century. As a check, we used present-day economic and population data to predict future changes in drought exposure. Although the specific numbers changed, we found similar spatial variations in drought exposure using either present-day (Fig. 12) or future (Fig. 8) GDP and population data. The main conclusion remains that low HDI countries bear the largest exacerbation in both economic and population exposures to drought extremes due to SAI (Fig. 13).

Despite these limitations, our multi-model ensemble projection presents a strong impact of SAI on global drought extremes and the consequent exposures for economy and population. As an effective intervention for global warming, SAI exhibits certain potentials in mitigating drought risks but with large spatial heterogeneity. Particularly, this study emphasizes the heightened vulnerability of low HDI countries to exacerbated drought exposures due to SAI. Future projections indicate that these regions, already at a socio-economic disadvantage, will face the most severe impacts on both economic development and public health. This spatial disparity underscores the importance of considering equity and regional specificities in SAI policies. As we navigate the complexities of geoengineering, it is imperative to weigh the global benefits against the localized risks, ensuring that strategies do not disproportionately burden the most vulnerable regions.

523 Author contributions. X.Y. conceived this research. C.T collected the data. W.F. 524 analyzed the data and wrote the draft paper. X.Y., R.X. and Y.G. reviewed and edited 525 the manuscript. 526 527 Financial support. This study was jointly funded by the National Key Research and 528 Development Program of China (2023YFF0805402), and Natural Science Foundation 529 of Jiangsu Province (BK20220031), and Postgraduate Research & Practice Innovation 530 Program of Jiangsu Province (KYCX25 1675). 531 532 **Competing interests.** The authors declare no conflicts of interest relevant to this study. 533 534 Data and code availability. The datasets are downloaded from the Coupled Model Intercomparison Project phase six (CMIP6, <a href="https://esgf-node.llnl.gov/search/cmip6/">https://esgf-node.llnl.gov/search/cmip6/</a>) 535 536 and Geoengineering Large Ensemble Project (GLENS. https://www.cesm.ucar.edu/community-projects/glens) for simulated meteorology, and 537 538 Climate Research Unit Gridded Time Series version4.07 (CRU TS4.07, https://crudata.uea.ac.uk/cru/data/hrg/) for observed meteorology. Population data are 539 540 collected from Socioeconomic Data and Applications Center (SEDAC, 541 https://sedac.ciesin.columbia.edu/). HDI data are from United Nations Development 542 Programme (UNDP, https://hdr.undp.org/). Code for calculating scPDSI can be found 543 at https://climate-indices.readthedocs.io/en/latest/. 544 Acknowledgements. The authors thank the CMIP6 for providing the GeoMIP6 545 546 datasets, the NCAR for the GLENS datasets, and the technical support of the National 547 Large Scientific and Technological Infrastructure "Earth System Numerical Simulation 548 Facility" (https://cstr.cn/31134.02.EL, last access: 11 August 2025). 549 550

#### 551 References

- Abiodun, B. J., Odoulami, R. C., Sawadogo, W., Oloniyo, O. A., Abatan, A. A., New, M.,
- 553 Lennard, C., Izidine, P., Egbebiyi, T. S., and MacMartin, D. G.: Potential impacts of
- stratospheric aerosol injection on drought risk managements over major river basins in Africa,
- 555 Climatic Change, 169, 31, <a href="https://doi.org/10.1007/s10584-021-03268-w">https://doi.org/10.1007/s10584-021-03268-w</a>, 2021.
- Allan, R., Pereira, L., and Smith, M.: Crop evapotranspiration-Guidelines for computing crop
- water requirements-FAO Irrigation and drainage paper 56, 1998.
- Alley, W. M.: The Palmer Drought Severity Index: Limitations and Assumptions, Journal of
- Applied Meteorology and Climatology, 23, 1100-1109, <a href="https://doi.org/10.1175/1520-">https://doi.org/10.1175/1520-</a>
- 560 <u>0450(1984)023</u><1100:TPDSIL>2.0.CO;2, 1984.
- Botai, C. M., Botai, J. O., De Wit, J. P., Ncongwane, K. P., and Adeola, A. M.: Drought
- Characteristics over the Western Cape Province, South Africa, 10.3390/w9110876, 2017.
- 563 Carrão, H., Naumann, G., and Barbosa, P.: Mapping global patterns of drought risk: An
- empirical framework based on sub-national estimates of hazard, exposure and vulnerability,
- 565 Global Environmental Change, 39, 108-124, <a href="https://doi.org/10.1016/j.gloenvcha.2016.04.012">https://doi.org/10.1016/j.gloenvcha.2016.04.012</a>,
- 566 2016.
- 567 Cheng, W., MacMartin, D. G., Kravitz, B., Visioni, D., Bednarz, E. M., Xu, Y., Luo, Y., Huang,
- L., Hu, Y., Staten, P. W., Hitchcock, P., Moore, J. C., Guo, A., and Deng, X.: Changes in Hadley
- 569 circulation and intertropical convergence zone under strategic stratospheric aerosol
- 570 geoengineering, npj Climate and Atmospheric Science, 5, 32, 10.1038/s41612-022-00254-6,
- 571 2022.
- 572 Dai, A.: Drought under global warming: a review, WIREs Climate Change, 2, 45-65,
- 573 <u>https://doi.org/10.1002/wcc.81</u>, 2011a.
- Dai, A.: Characteristics and trends in various forms of the Palmer Drought Severity Index
- 575 during 1900–2008, Journal of Geophysical Research, 116,
- 576 <a href="https://doi.org/10.1029/2010JD015541">https://doi.org/10.1029/2010JD015541</a>, 2011b.
- Dai, A.: Increasing drought under global warming in observations and models, Nature Climate
- 578 Change, 3, 52-58, https://doi.org/10.1038/nclimate1633, 2013.
- 579 Dellink, R., Chateau, J., Lanzi, E., and Magné, B.: Long-term economic growth projections in
- 580 the Shared Socioeconomic Pathways, Global Environmental Change, 42, 200-214,
- 581 https://doi.org/10.1016/j.gloenvcha.2015.06.004, 2017.
- 582 Diallo, H. A.: United Nations convention to Combat desertification (UNCCD), The Future of
- 583 Drylands: International Scientific Conference on Desertification and Drylands Research Tunis,
- 584 Tunisia, 19-21 June 2006, 13-16,
- 585 Diffenbaugh, N. S., Scherer, M., and Ashfaq, M.: Response of snow-dependent hydrologic
- 586 extremes to continued global warming, Nature Climate Change, 3, 379-384,
- 587 10.1038/nclimate1732, 2013.
- Du, H., Tan, M. L., Samat, N., Chen, Z., and Zhang, F.: Integrating a comprehensive index and
- 589 the SWAT+ model to assess drought characteristics and risks under solar radiation modification,
- 590 Ecological Indicators, 178, 113852, https://doi.org/10.1016/j.ecolind.2025.113852, 2025.
- Duffey, A. and Irvine, P. J.: Accounting for transience in the baseline climate state changes the
- surface climate response attributed to stratospheric aerosol injection, Environmental Research:
- 593 Climate, 3, 041008, 10.1088/2752-5295/ad9f91, 2024.
- English, J. M., Toon, O. B., and Mills, M. J.: Microphysical simulations of sulfur burdens from
- 595 stratospheric sulfur geoengineering, Atmospheric Chemistry and Physics., 12, 4775-4793,
- 596 10.5194/acp-12-4775-2012, 2012.
- 597 Ferraro, A. J., Highwood, E. J., and Charlton-Perez, A. J.: Weakened tropical circulation and
- reduced precipitation in response to geoengineering, Environmental Research Letters, 9,
- 599 014001, 10.1088/1748-9326/9/1/014001, 2014.
- 600 Geiger, T.: Continuous national gross domestic product (GDP) time series for 195 countries:
- past observations (1850–2005) harmonized with future projections according to the Shared
- 602 Socio-economic Pathways (2006-2100), Earth System. Science. Data, 10, 847-856,
- 603 10.5194/essd-10-847-2018, 2018.

- Harris, I., Osborn, T. J., Jones, P., and Lister, D.: Version 4 of the CRU TS monthly high-
- resolution gridded multivariate climate dataset, Scientific Data, 7, 109, 10.1038/s41597-020-
- 606 0453-3, 2020.
- Held, I. M. and Soden, B. J.: Robust Responses of the Hydrological Cycle to Global Warming,
- 508 Journal of Climate, 19, 5686-5699, https://doi.org/10.1175/JCLI3990.1, 2006.
- 609 Irvine, P., Emanuel, K., He, J., Horowitz, L. W., Vecchi, G., and Keith, D.: Halving warming
- with idealized solar geoengineering moderates key climate hazards, Nature Climate Change, 9,
- 611 295-299, <a href="https://doi.org/10.1038/s41558-019-0398-8">https://doi.org/10.1038/s41558-019-0398-8</a>, 2019.
- 612 Irvine, P. J., Sriver, R. L., and Keller, K.: Tension between reducing sea-level rise and global
- 613 warming through solar-radiation management, Nature Climate Change, 2, 97-100,
- 614 10.1038/nclimate1351, 2012.
- Jiang, J., Xia, Y., Cao, L., Kravitz, B., MacMartin, D. G., Fu, J., and Jiang, G.: Different
- 616 Strategies of Stratospheric Aerosol Injection Would Significantly Affect Climate Extreme
- Mitigation, Earth's Future, 12, e2023EF004364, <a href="https://doi.org/10.1029/2023EF004364">https://doi.org/10.1029/2023EF004364</a>, 2024.
- Jones, A., Haywood, J. M., Scaife, A. A., Boucher, O., Henry, M., Kravitz, B., Lurton, T., Nabat,
- P., Niemeier, U., Séférian, R., Tilmes, S., and Visioni, D.: The impact of stratospheric aerosol
- intervention on the North Atlantic and Quasi-Biennial Oscillations in the Geoengineering
- Model Intercomparison Project (GeoMIP) G6sulfur experiment, Atmospheric Chemistry and
- 622 Physics, 22, 2999-3016, 10.5194/acp-22-2999-2022, 2022.
- Jones, A. C., Haywood, J. M., Dunstone, N., Emanuel, K., Hawcroft, M. K., Hodges, K. I., and
- Jones, A.: Impacts of hemispheric solar geoengineering on tropical cyclone frequency, Nature
- 625 Communications, 8, 1382, 10.1038/s41467-017-01606-0, 2017.
- Jones, B. and O'Neill, B. C.: Spatially Explicit Global Population Scenarios Consistent with the
- 627 Shared Socioeconomic Pathways, Environmental Research Letters, 2016.
- Jones, B. and O'Neill, B. C.: Global One-Eighth Degree Population Base Year and Projection
- 629 Grids Based on the Shared Socioeconomic Pathways, Revision 01, NASA Socioeconomic Data
- and Applications Center (SEDAC) [dataset], 2020.
- Karami, K., Tilmes, S., Muri, H., and Mousavi, S. V.: Storm Track Changes in the Middle East
- and North Africa Under Stratospheric Aerosol Geoengineering, Geophysical Research Letters,
- 633 47, e2020GL086954, https://doi.org/10.1029/2020GL086954, 2020.
- Kendon, E. J., Stratton, R. A., Tucker, S., Marsham, J. H., Berthou, S., Rowell, D. P., and Senior,
- 635 C. A.: Enhanced future changes in wet and dry extremes over Africa at convection-permitting
- 636 scale, Nature Communications, 10, 1794, 10.1038/s41467-019-09776-9, 2019.
- Kravitz, B., Robock, A., Boucher, O., Schmidt, H., Taylor, K. E., Stenchikov, G., and Schulz,
- 638 M.: The Geoengineering Model Intercomparison Project (GeoMIP), Atmospheric Science
- 639 Letters, 12, 162-167, https://doi.org/10.1002/asl.316, 2011.
- Kravitz, B., MacMartin, D. G., Mills, M. J., Richter, J. H., Tilmes, S., Lamarque, J.-F., Tribbia,
- J. J., and Vitt, F.: First Simulations of Designing Stratospheric Sulfate Aerosol Geoengineering
- 642 to Meet Multiple Simultaneous Climate Objectives, Journal of Geophysical Research:
- 643 Atmospheres, 122, 12,616-612,634, https://doi.org/10.1002/2017JD026874, 2017.
- Kravitz, B., Robock, A., Tilmes, S., Boucher, O., English, J. M., Irvine, P. J., Jones, A.,
- Lawrence, M. G., MacCracken, M., Muri, H., Moore, J. C., Niemeier, U., Phipps, S. J., Sillmann,
- J., Storelvmo, T., Wang, H., and Watanabe, S.: The Geoengineering Model Intercomparison
- 647 Project Phase 6 (GeoMIP6): simulation design and preliminary results, Geosci. Model Dev., 8,
- 648 3379-3392, 10.5194/gmd-8-3379-2015, 2015.
- Krishnamohan, K. S. and Bala, G.: Sensitivity of tropical monsoon precipitation to the latitude
- of stratospheric aerosol injections, Climate Dynamics, 59, 151-168, 10.1007/s00382-021-
- 651 06121-z, 2022.
- 652 Liu, Z., Lang, X., and Jiang, D.: Stratospheric Aerosol Injection Geoengineering Would
- 653 Mitigate Greenhouse Gas-Induced Drying and Affect Global Drought Patterns, Journal of
- 654 Geophysical Research: Atmospheres, 129, e2023JD039988,
- 655 https://doi.org/10.1029/2023JD039988, 2024.

- 656 MacMartin, D. G. and Kravitz, B.: Mission-driven research for stratospheric aerosol
- 657 geoengineering, Proceedings of the National Academy of Sciences, 116, 1089-1094,
- 658 10.1073/pnas.1811022116, 2019.
- Mauritsen, T., Bader, J., Becker, T., Behrens, J., Bittner, M., Brokopf, R., Brovkin, V., Claussen,
- M., Crueger, T., Esch, M., Fast, I., Fiedler, S., Fläschner, D., Gayler, V., Giorgetta, M., Goll, D.
- 661 S., Haak, H., Hagemann, S., Hedemann, C., Hohenegger, C., Ilyina, T., Jahns, T., Jimenéz-de-
- la-Cuesta, D., Jungclaus, J., Kleinen, T., Kloster, S., Kracher, D., Kinne, S., Kleberg, D.,
- 663 Lasslop, G., Kornblueh, L., Marotzke, J., Matei, D., Meraner, K., Mikolajewicz, U., Modali,
- K., Möbis, B., Müller, W. A., Nabel, J. E. M. S., Nam, C. C. W., Notz, D., Nyawira, S.-S.,
- Paulsen, H., Peters, K., Pincus, R., Pohlmann, H., Pongratz, J., Popp, M., Raddatz, T. J., Rast,
- 666 S., Redler, R., Reick, C. H., Rohrschneider, T., Schemann, V., Schmidt, H., Schnur, R.,
- 667 Schulzweida, U., Six, K. D., Stein, L., Stemmler, I., Stevens, B., von Storch, J.-S., Tian, F.,
- Voigt, A., Vrese, P., Wieners, K.-H., Wilkenskjeld, S., Winkler, A., and Roeckner, E.:
- Developments in the MPI-M Earth System Model version 1.2 (MPI-ESM1.2) and Its Response
- 670 to Increasing CO2, Journal of Advances in Modeling Earth Systems, 11, 998-1038,
- 671 https://doi.org/10.1029/2018MS001400, 2019.
- Monteith, J. L.: Evaporation and environment, Symposia of the Society for Experimental
- 673 Biology, 19, 205-234, 1965.
- Niemeier, U., Richter, J. H., and Tilmes, S.: Differing responses of the quasi-biennial oscillation
- to artificial SO2 injections in two global models, Atmos. Chem. Phys., 20, 8975-8987,
- 676 10.5194/acp-20-8975-2020, 2020.
- Niemeier, U., Schmidt, H., Alterskjær, K., and Kristjánsson, J. E.: Solar irradiance reduction
- of the energy balance and the
- hydrological cycle, Journal of Geophysical Research: Atmospheres, 118, 11,905-911,917,
- 680 https://doi.org/10.1002/2013JD020445, 2013.
- Odoulami, R. C., New, M., Wolski, P., Guillemet, G., Pinto, I., Lennard, C., Muri, H., and
- Tilmes, S.: Stratospheric Aerosol Geoengineering could lower future risk of 'Day Zero' level
- droughts in Cape Town, Environmental Research Letters, 15, 124007, 10.1088/1748-
- 684 9326/abbf13, 2020.
- Palmer, P. I., Wainwright, C. M., Dong, B., Maidment, R. I., Wheeler, K. G., Gedney, N.,
- Hickman, J. E., Madani, N., Folwell, S. S., Abdo, G., Allan, R. P., Black, E. C. L., Feng, L.,
- 687 Gudoshava, M., Haines, K., Huntingford, C., Kilavi, M., Lunt, M. F., Shaaban, A., and Turner,
- 688 A. G.: Drivers and impacts of Eastern African rainfall variability, Nature Reviews Earth &
- 689 Environment, 4, 254-270, 10.1038/s43017-023-00397-x, 2023.
- 690 Penman, H. L. and Keen, B. A.: Natural evaporation from open water, bare soil and grass,
- 691 Proceedings of the Royal Society of London. Series A. Mathematical and Physical Sciences,
- 692 193, 120-145, 10.1098/rspa.1948.0037, 1948.
- 693 Pope, F. D., Braesicke, P., Grainger, R. G., Kalberer, M., Watson, I. M., Davidson, P. J., and
- 694 Cox, R. A.: Stratospheric aerosol particles and solar-radiation management, Nature Climate
- 695 Change, 2, 713-719, 10.1038/nclimate1528, 2012.
- 696 Rezaei, A., Moore, J., Tilmes, S., and Karami, K.: Regional and Seasonal Hydrological Changes
- 697 With and Without Stratospheric Aerosol Intervention Under High Greenhouse Gas Climates,
- 698 Journal of Geophysical Research: Atmospheres, 130, e2025JD044163,
- 699 https://doi.org/10.1029/2025JD044163, 2025.
- Ricke, K., Wan, J. S., Saenger, M., and Lutsko, N. J.: Hydrological Consequences of Solar
- 701 Geoengineering, 51, 447-470, https://doi.org/10.1146/annurev-earth-031920-083456, 2023.
- Ricke, K. L., Rowlands, D. J., Ingram, W. J., Keith, D. W., and Granger Morgan, M.:
- 703 Effectiveness of stratospheric solar-radiation management as a function of climate sensitivity,
- Nature Climate Change, 2, 92-96, 10.1038/nclimate1328, 2012.
- Rusca, M., Savelli, E., Di Baldassarre, G., Biza, A., and Messori, G.: Unprecedented droughts
- are expected to exacerbate urban inequalities in Southern Africa, Nature Climate Change, 13,
- 707 98-105, 10.1038/s41558-022-01546-8, 2023.

- Samaniego, L., Thober, S., Kumar, R., Wanders, N., Rakovec, O., Pan, M., Zink, M., Sheffield,
- J., Wood, E. F., and Marx, A.: Anthropogenic warming exacerbates European soil moisture
- droughts, Nature Climate Change, 8, 421-426, 10.1038/s41558-018-0138-5, 2018.
- 711 Simpson, I. R., Tilmes, S., Richter, J. H., Kravitz, B., MacMartin, D. G., Mills, M. J., Fasullo,
- 712 J. T., and Pendergrass, A. G.: The Regional Hydroclimate Response to Stratospheric Sulfate
- Geoengineering and the Role of Stratospheric Heating, Journal of Geophysical Research:
- 714 Atmospheres, 124, 12587-12616, https://doi.org/10.1029/2019JD031093, 2019.
- 715 Smith, A.: The Atlas of Mortality and Economic Losses from Weather, Climate and Water
- 716 Extremes (1970–2019), 2021.
- Smith, W.: The cost of stratospheric aerosol injection through 2100, Environmental Research
- 718 Letters, 15, 114004, 10.1088/1748-9326/aba7e7, 2020.
- 719 Smith, W. and Wagner, G.: Stratospheric aerosol injection tactics and costs in the first 15 years
- 720 of deployment, Environmental Research Letters, 13, 124001, 10.1088/1748-9326/aae98d, 2018.
- Song, F., Zhang, G. J., Ramanathan, V., and Leung, L. R.: Trends in surface equivalent potential
- 722 temperature: A more comprehensive metric for global warming and weather extremes,
- Proceedings of the National Academy of Sciences, 119, 10.1073/pnas.2117832119, 2022.
- Sun, F., Wang, T., and Wang, H.: Mapping Global GDP Exposure to Drought, in: Atlas of Global
- 725 Change Risk of Population and Economic Systems, Springer Nature Singapore, Singapore,
- 726 123-130, 10.1007/978-981-16-6691-9 9, 2022.
- 727 Taylor, K. E.: Summarizing multiple aspects of model performance in a single diagram, Journal
- 728 of Geophysical Research: Atmospheres, 106, 7183-7192,
- 729 https://doi.org/10.1029/2000JD900719, 2001.
- 730 Tebaldi, C., Ranasinghe, R., Vousdoukas, M., Rasmussen, D. J., Vega-Westhoff, B., Kirezci, E.,
- Kopp, R. E., Sriver, R., and Mentaschi, L.: Extreme sea levels at different global warming levels,
- 732 Nature Climate Change, 11, 746-751, 10.1038/s41558-021-01127-1, 2021.
- 733 Thornthwaite, C. W.: An Approach toward a Rational Classification of Climate, Geographical
- 734 Review, 38, 55-94, 10.2307/210739, 1948.
- 735 Tilmes, S., Mills, M. J., Niemeier, U., Schmidt, H., Robock, A., Kravitz, B., Lamarque, J. F.,
- Pitari, G., and English, J. M.: A new Geoengineering Model Intercomparison Project (GeoMIP)
- experiment designed for climate and chemistry models, Geosci. Model Dev., 8, 43-49,
- 738 10.5194/gmd-8-43-2015, 2015.
- 739 Tilmes, S., Richter, J. H., Kravitz, B., MacMartin, D. G., Mills, M. J., Simpson, I. R., Glanville,
- A. S., Fasullo, J. T., Phillips, A. S., Lamarque, J.-F., Tribbia, J., Edwards, J., Mickelson, S., and
- 741 Ghosh, S.: CESM1(WACCM) Stratospheric Aerosol Geoengineering Large Ensemble Project,
- Hulletin of the American Meteorological Society, 99, 2361-2371, 10.1175/bams-d-17-0267.1,
- 743 2018.
- Tilmes, S., Fasullo, J., Lamarque, J.-F., Marsh, D. R., Mills, M., Alterskjær, K., Muri, H.,
- Kristjánsson, J. E., Boucher, O., Schulz, M., Cole, J. N. S., Curry, C. L., Jones, A., Haywood,
- 746 J., Irvine, P. J., Ji, D., Moore, J. C., Karam, D. B., Kravitz, B., Rasch, P. J., Singh, B., Yoon, J.-
- H., Niemeier, U., Schmidt, H., Robock, A., Yang, S., and Watanabe, S.: The hydrological impact
- of geoengineering in the Geoengineering Model Intercomparison Project (GeoMIP), Journal of
- 749 Geophysical Research: Atmospheres, 118, 11,036-011,058, <a href="https://doi.org/10.1002/jgrd.50868">https://doi.org/10.1002/jgrd.50868</a>,
- 750 2013.
- 751 Tilmes, S., Visioni, D., Jones, A., Haywood, J., Séférian, R., Nabat, P., Boucher, O., Bednarz,
- 752 E. M., and Niemeier, U.: Stratospheric ozone response to sulfate aerosol and solar dimming
- 753 climate interventions based on the G6 Geoengineering Model Intercomparison Project
- 754 (GeoMIP) simulations, Atmos. Chem. Phys., 22, 4557-4579, 10.5194/acp-22-4557-2022, 2022.
- 755 Trenberth, K. E., Dai, A., van der Schrier, G., Jones, P. D., Barichivich, J., Briffa, K. R., and
- 756 Sheffield, J.: Global warming and changes in drought, Nature Climate Change, 4, 17-22,
- 757 10.1038/nclimate2067, 2014.
- 758 UNDP: Human Development Report 2023/2024: breaking the gridlock reimagining
- 759 cooperation in a polarized world, New York, 2024.

- van der Schrier, G., Barichivich, J., Briffa, K. R., and Jones, P. D.: A scPDSI-based global data
- set of dry and wet spells for 1901–2009, Journal of Geophysical Research: Atmospheres, 118,
- 762 4025-4048, https://doi.org/10.1002/jgrd.50355, 2013.
- Visioni, D., MacMartin, D. G., Kravitz, B., Boucher, O., Jones, A., Lurton, T., Martine, M.,
- Mills, M. J., Nabat, P., Niemeier, U., Séférian, R., and Tilmes, S.: Identifying the sources of
- uncertainty in climate model simulations of solar radiation modification with the G6sulfur and
- 766 G6solar Geoengineering Model Intercomparison Project (GeoMIP) simulations, Atmos. Chem.
- 767 Phys., 21, 10039-10063, 10.5194/acp-21-10039-2021, 2021.
- Visioni, D., Kravitz, B., Robock, A., Tilmes, S., Haywood, J., Boucher, O., Lawrence, M.,
- 769 Irvine, P., Niemeier, U., Xia, L., Chiodo, G., Lennard, C., Watanabe, S., Moore, J. C., and Muri,
- 770 H.: Opinion: The scientific and community-building roles of the Geoengineering Model
- 771 Intercomparison Project (GeoMIP) past, present, and future, Atmos. Chem. Phys., 23, 5149-
- 772 5176, 10.5194/acp-23-5149-2023, 2023.
- Wang, T. and Sun, F.: Global gridded GDP data set consistent with the shared socioeconomic
- 774 pathways, Scientific Data, 9, 221, 10.1038/s41597-022-01300-x, 2022.
- Webb, R., Rosenzweig, C. E., and Levine, E. R.: Global Soil Texture and Derived Water-
- Holding Capacities (Webb et al.), 10.3334/ORNLDAAC/548, 2000.
- Wells, N., Goddard, S., and Hayes, M. J.: A Self-Calibrating Palmer Drought Severity Index,
- 778 Journal of Climate, 17, 2335-2351, <a href="https://doi.org/10.1175/1520-">https://doi.org/10.1175/1520-</a>
- 779 <u>0442(2004)017</u><2335:ASPDSI>2.0.CO;2, 2004.
- Wilson, J. C., Jonsson, H. H., Brock, C. A., Toohey, D. W., Avallone, L. M., Baumgardner, D.,
- 781 Dye, J. E., Poole, L. R., Woods, D. C., DeCoursey, R. J., Osborn, M., Pitts, M. C., Kelly, K. K.,
- 782 Chan, K. R., Ferry, G. V., Loewenstein, M., Podolske, J. R., and Weaver, A.: In Situ
- 783 Observations of Aerosol and Chlorine Monoxide After the 1991 Eruption of Mount Pinatubo:
- 784 Effect of Reactions on Sulfate Aerosol, Science, 261, 1140-1143,
- 785 10.1126/science.261.5125.1140, 1993.
- Yue, X., Tian, C., and Lei, Y.: Relieved drought in China under a low emission pathway to
- 787 1.5°C global warming, International Journal of Climatology, 41, E259-E270,
- 788 <u>https://doi.org/10.1002/joc.6682</u>, 2021.

- 789 Zhao, M., Cao, L., Bala, G., and Duan, L.: Climate Response to Latitudinal and Altitudinal
- 790 Distribution of Stratospheric Sulfate Aerosols, Journal of Geophysical Research: Atmospheres,
- 791 126, e2021JD035379, https://doi.org/10.1029/2021JD035379, 2021.
- 792 Zhou, L., Tian, Y., Myneni, R. B., Ciais, P., Saatchi, S., Liu, Y. Y., Piao, S., Chen, H., Vermote,
- 793 E. F., Song, C., and Hwang, T.: Widespread decline of Congo rainforest greenness in the past
- 794 decade, Nature, 509, 86-90, 10.1038/nature13265, 2014.



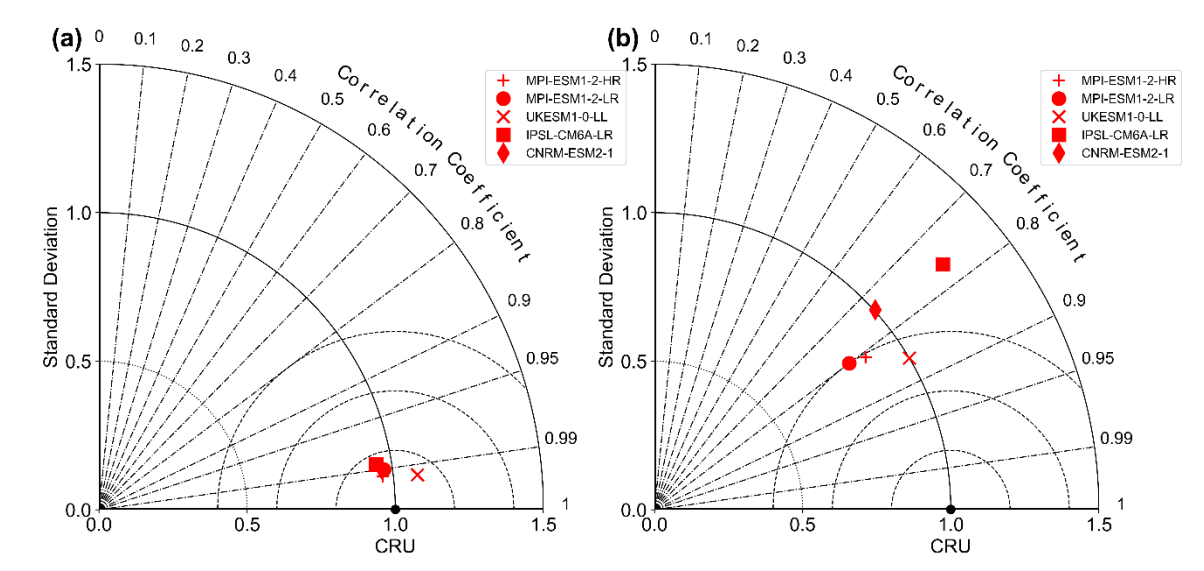


**Figure 1.** Evaluation of climate models from GeoMIP6. Results shown are the Taylor diagram of annual mean (a) temperature and (b) precipitation for GeoMIP6 models during the period of 1995–2014.



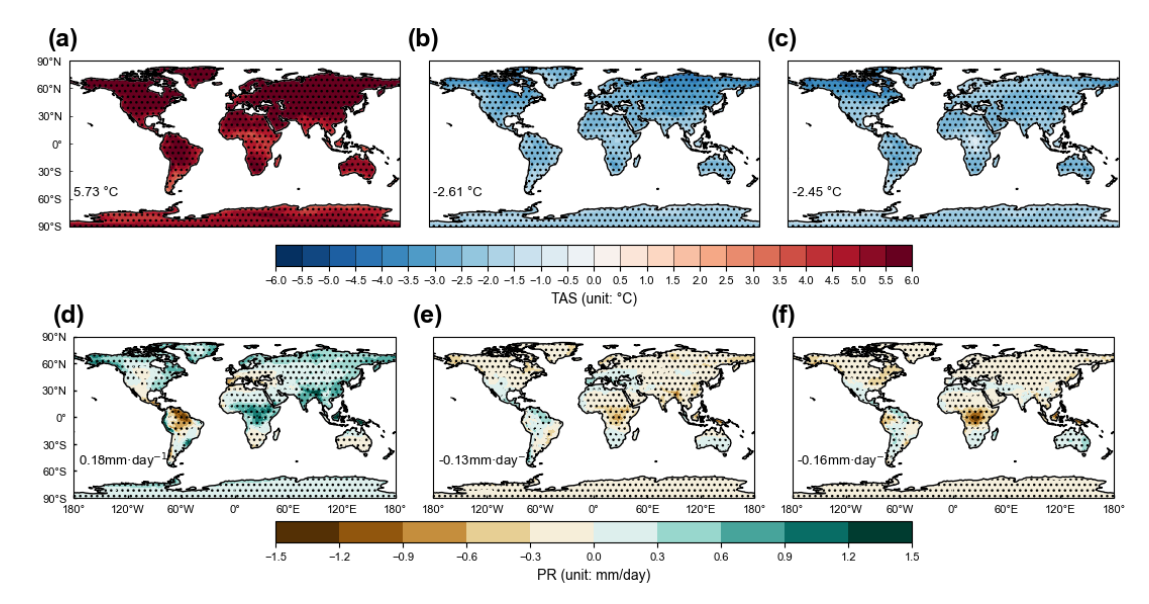
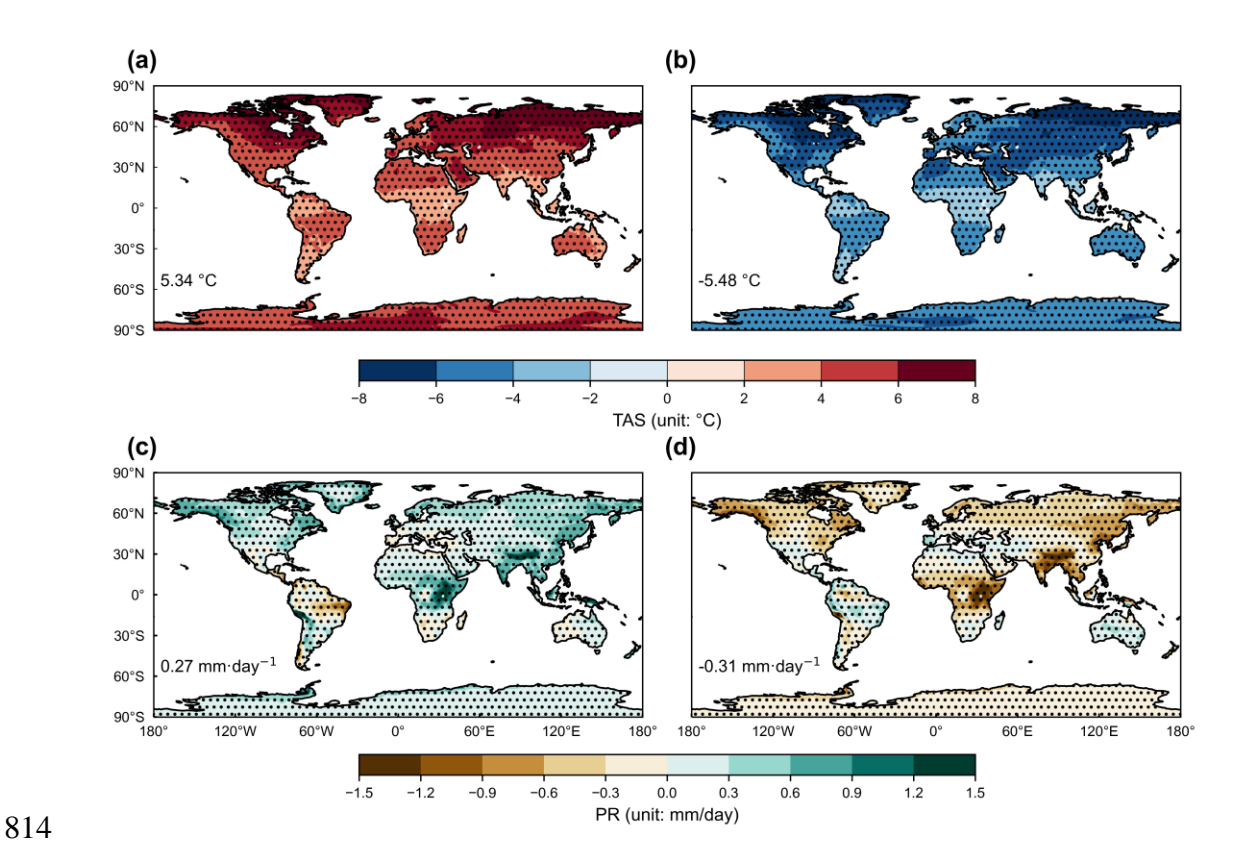


Figure 2. Climatic responses to global warming and SRM in GeoMIP. Results shown are the spatial pattern of annual mean changes in (a, b, c) surface air temperature (TAS) and (d, e, f) precipitation (PR) at 2081-2100 under (a, d) SSP5-8.5 scenario relative to the historical period of 1995-2014, as well as that under (b, e) G6solar and (c, f) G6sulfur scenarios relative to SSP5-8.5 both at 2081-2100. The dotted areas indicate regions where at least four out of five models show changes with the same signs. The mean value of the difference over global land surface is shown at the lower-left of each panel.



**Figure 3**. Climatic responses to global warming and SAI in GLENS. Results shown are the spatial pattern of annual mean changes in (a, b) temperature (TAS) and (c, d) precipitation (PR) at 2075-2094 under (a, c) RCP8.5 scenario relative to 2010-2030 baseline, as well as that under (b, d) SAI scenarios relative to RCP8.5 at 2075-2094. The dotted areas indicate regions where at least two out of three members show changes with the same signs. The mean value of the difference over global land surface is shown at the lower left of each panel.

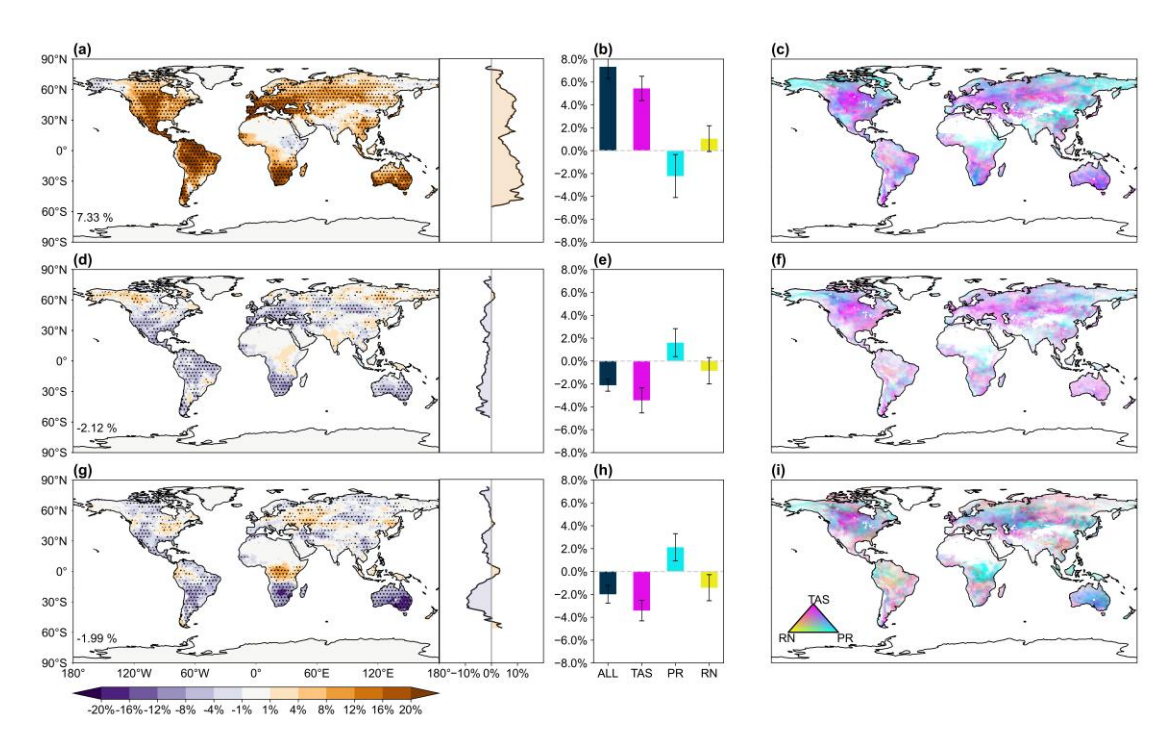
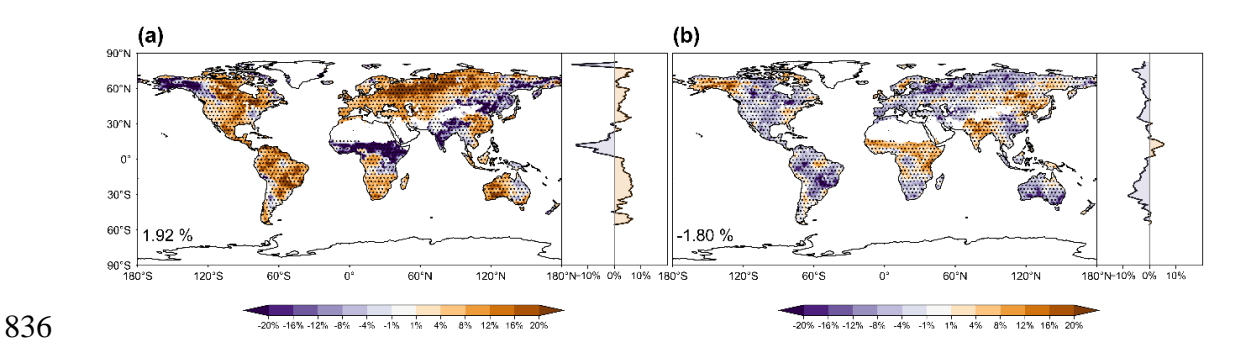
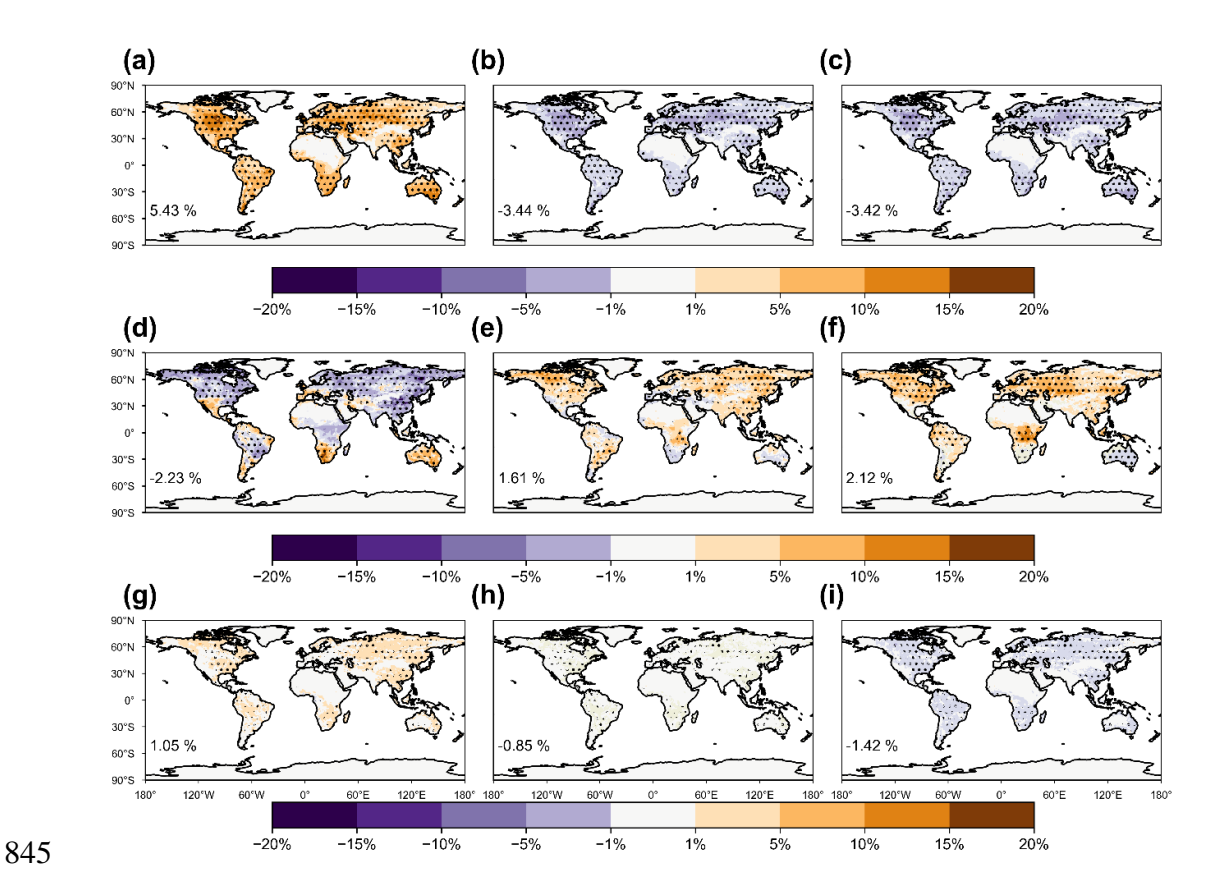


Figure 4. Changes in frequency of drought extremes by global warming and SRM in GeoMIP. Results shown are the changes in frequency of drought extremes (scPDSI < -4) at 2081-2100 under (a) SSP5-8.5 scenario relative to the historical period of 1995-2014, as well as that under (d) G6solar and (g) G6sulfur scenarios relative to SSP5-8.5 both at 2081-2100. The dotted areas indicate regions where at least four out of five models show changes with the same signs. Latitudinal distribution is shown on the right of each panel. Contributions of temperature (TAS), precipitation (PR), and radiation (RN) to changes in drought extremes are also presented, with bars in (b, e, h) representing the mean and errorbars indicating one standard deviation of predictions from five GeoMIP models. Colors in (c, f, i) indicate the dominant drivers of drought extremes.



**Figure 5.** Changes in frequency of drought extremes by global warming and SAI in GLENS. Results shown are the changes in frequency of drought extremes (scPDSI < -4) at 2075-2094 under (a) RCP8.5 scenario relative to 2010-2030 baseline, as well as that under (b) SAI scenarios relative to RCP8.5 at 2075-2094. The dotted areas indicate regions where at least two out of three members show changes with the same signs. Latitudinal distribution is shown on the right of each panel. The global mean value of the difference is shown at the lower left of each panel.



**Figure 6**. Changes in frequency of drought extremes due to different climatic factors. Results shown are the changes in frequency of drought extremes (scPDSI < -4) at 2081-2100 under SSP5-8.5 scenario relative to the historical period of 1995-2014 attributable to (a) temperature, (d) precipitation, and (g) radiation changes, as well as that under (b, e, h) G6solar and (c, f, i) G6sulfur scenarios relative to SSP5-8.5 both at 2081-2100 attributable to (b, c) temperature, (e, f) precipitation, and (h, i) radiation changes. The dotted areas indicate regions where at least four out of five models show changes with the same signs.

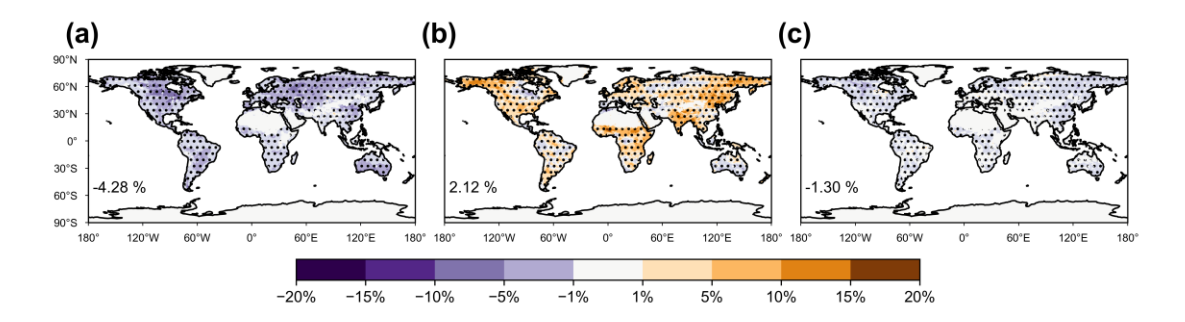


**Figure 7**. The same as Figure 6 but GLENS is applied. Results shown are the changes in frequency of drought extremes (scPDSI < -4) under SAI scenarios relative to RCP8.5 at 2075-2094 attributable to (a) temperature, (b) precipitation, and (c) radiation changes.

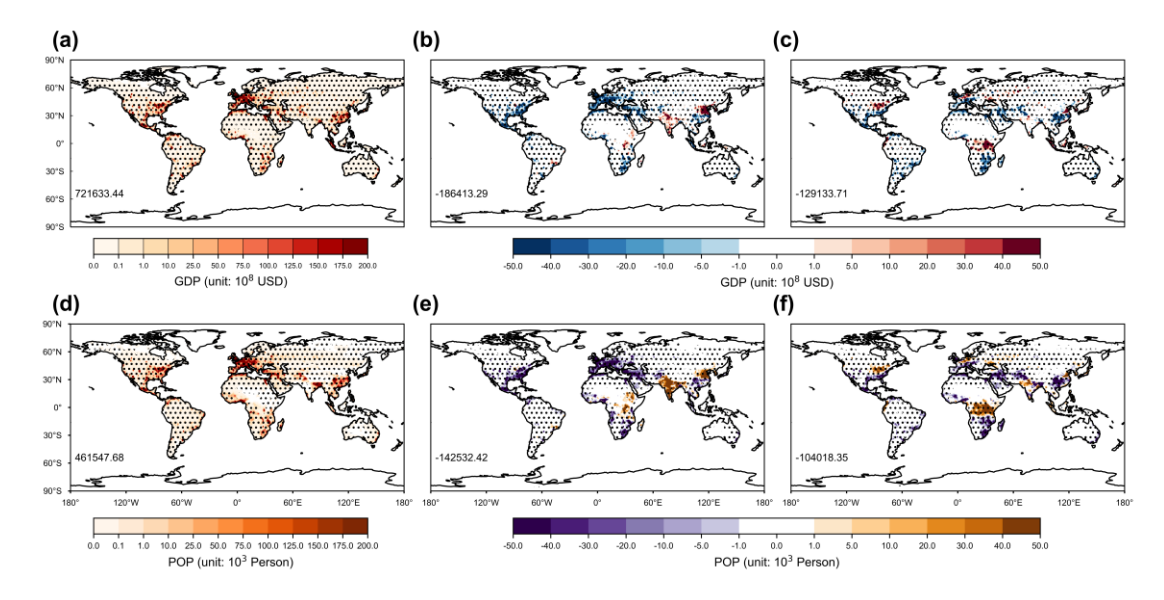
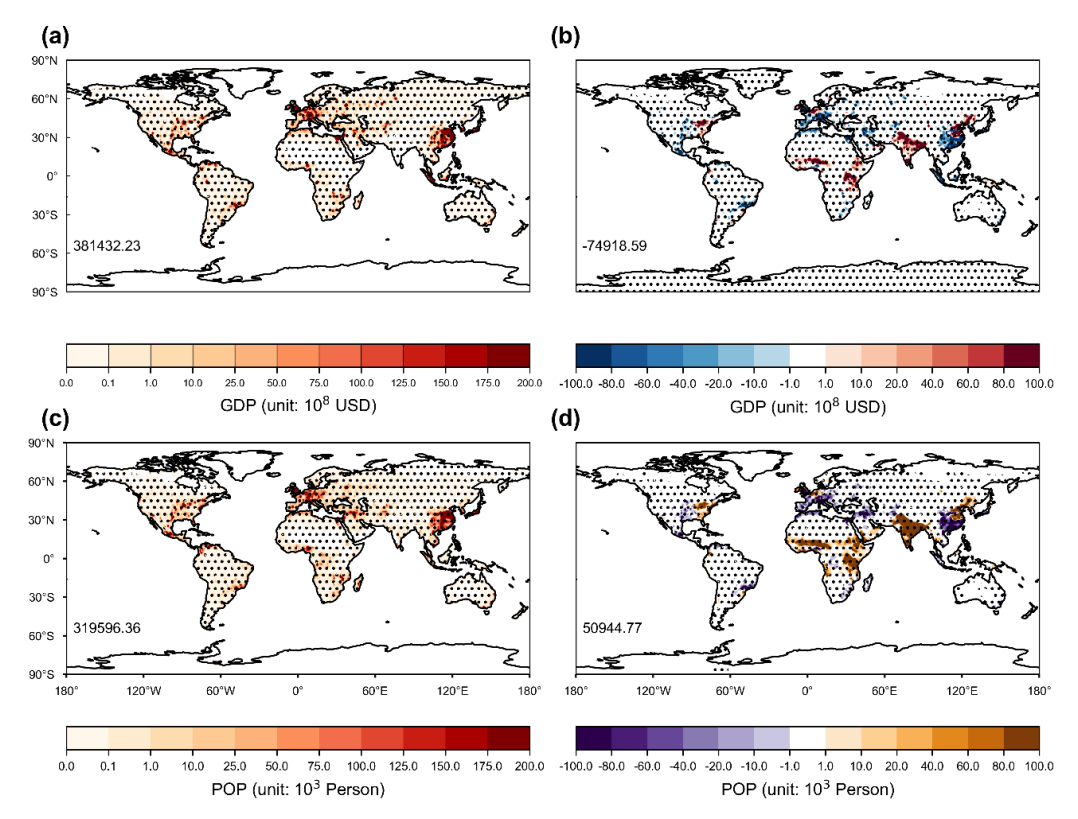


Figure 8. Changes in GDP and population exposure to drought extremes. Results shown are the changes of (a, b, c) GDP and (c, d, f) population (POP) exposure to drought extremes at 2081-2100 (a, d) under SSP5-8.5 scenario relative to the historical period of 1995-2014, as well as that (b, e) under G6solar and (c, f) G6sulfur scenarios relative to SSP5-8.5 both at 2081-2100. The dotted areas indicate regions where at least four out of five models show changes with the same signs. The global sum value of the difference is shown at the lower-left of each panel.



**Figure 9.** Changes in GDP and population exposure to drought extremes by global warming and SAI in GLENS. Results shown are the changes of (a, b) GDP and (c, d) population (POP) exposure to drought extremes at 2075-2094 (a, c) under RCP8.5 scenario relative to 2010-2030 baseline, as well as that (b, d) under SAI scenarios relative to control both at 2075-2094. The dotted areas indicate regions where at least two out of three models show changes with the same signs. The global mean value of the difference is shown at the lower left of each panel.

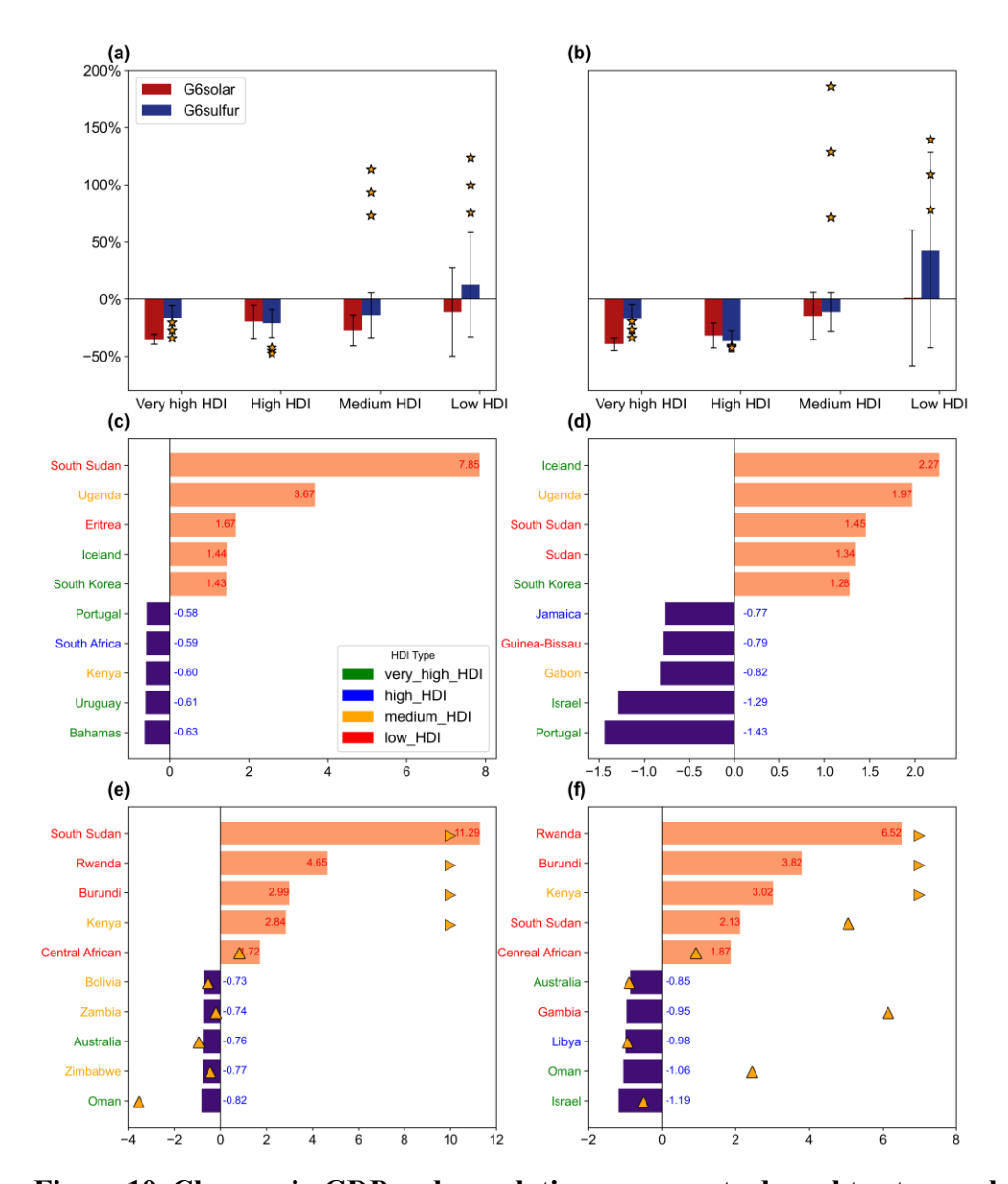
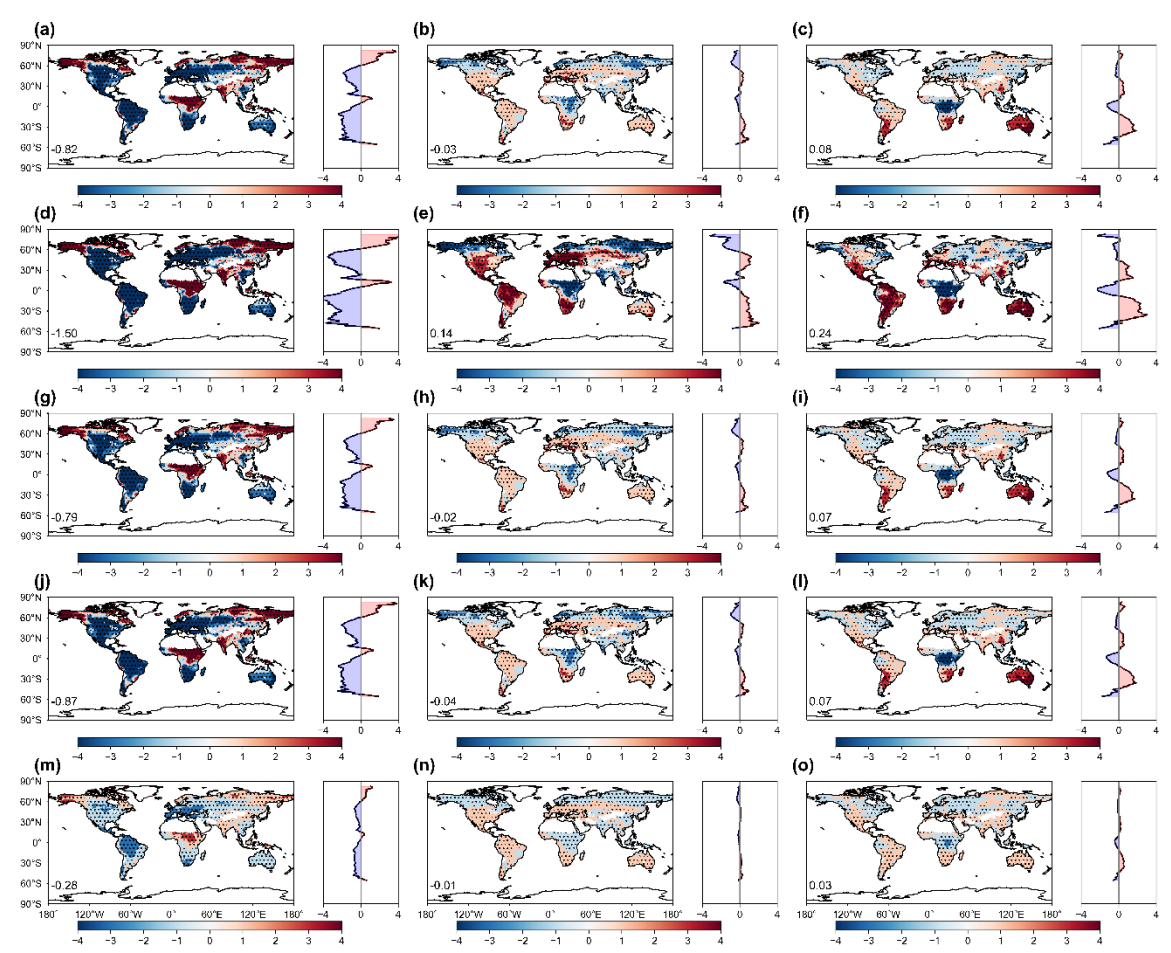


Figure 10. Changes in GDP and population exposure to drought extremes by HDI.

For each of four HDI groups, changes in (a) GDP or (b) population exposure to drought extremes for 2081-2100 in G6solar (blue) and G6sulfur (red) relative to SSP5-8.5 are normalized by the differences under SSP5-8.5 relative to 1995-2014. The bars represent the mean changes from five models with errorbars indicating one standard deviation for inter-model spread. Yellow stars represent results from three members of GLENS. The mitigation potential (MP, see Methods) is also calculated for individual countries, and the top 5 countries with the greatest mitigation (violet) or aggravation (orange) of (c, e) GDP and (d, f) population exposures to drought extremes are shown for (c, d) G6solar and (e, f) G6sulfur, respectively. The MP values (ratios of changes) are denoted for those top countries. Yellow triangles denote GLENS outcomes (right-aligned for values exceeding axis limits).



**Figure 11.** Change of drought status indicated by different indices. Results shown are the changes of drought indices (a, d, g, j, m) at 2081-2100 under SSP5-8.5 scenario relative to the historical period of 1995-2014, as well as that under (b, e, h, k, n) G6solar and (c, f, i, l, o) G6sulfur scenarios relative to SSP5-8.5 both at 2081-2100. Drought indices include (a, b, c) self-calibrating Palmer Drought Severity Index (scPDSI), (d, e, f) PDSI, (g, h, i) Palmer Modified Drought Index (PMDI), (j, k, l) Palmer Hydrological Drought Index (PHDI), and (m, n, o) Palmer Z Index. The latitudinal distribution of the changes is shown on the right side of each panel. The dotted areas indicate regions where at least four out of five models show changes with the same signs.

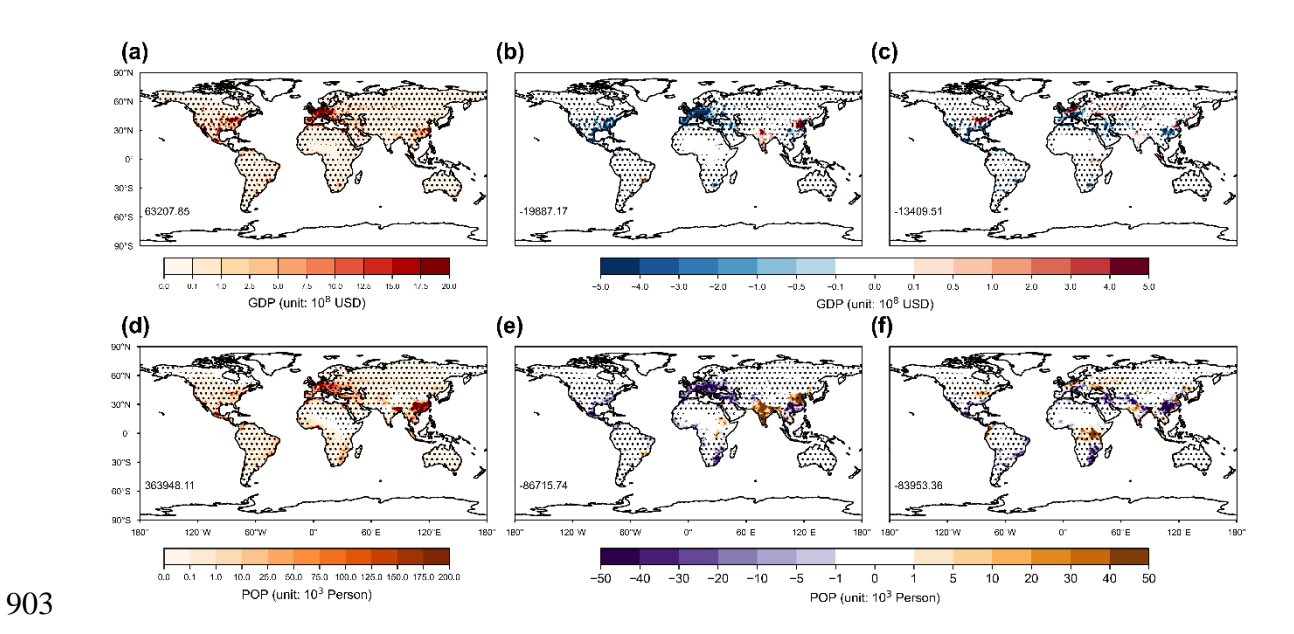
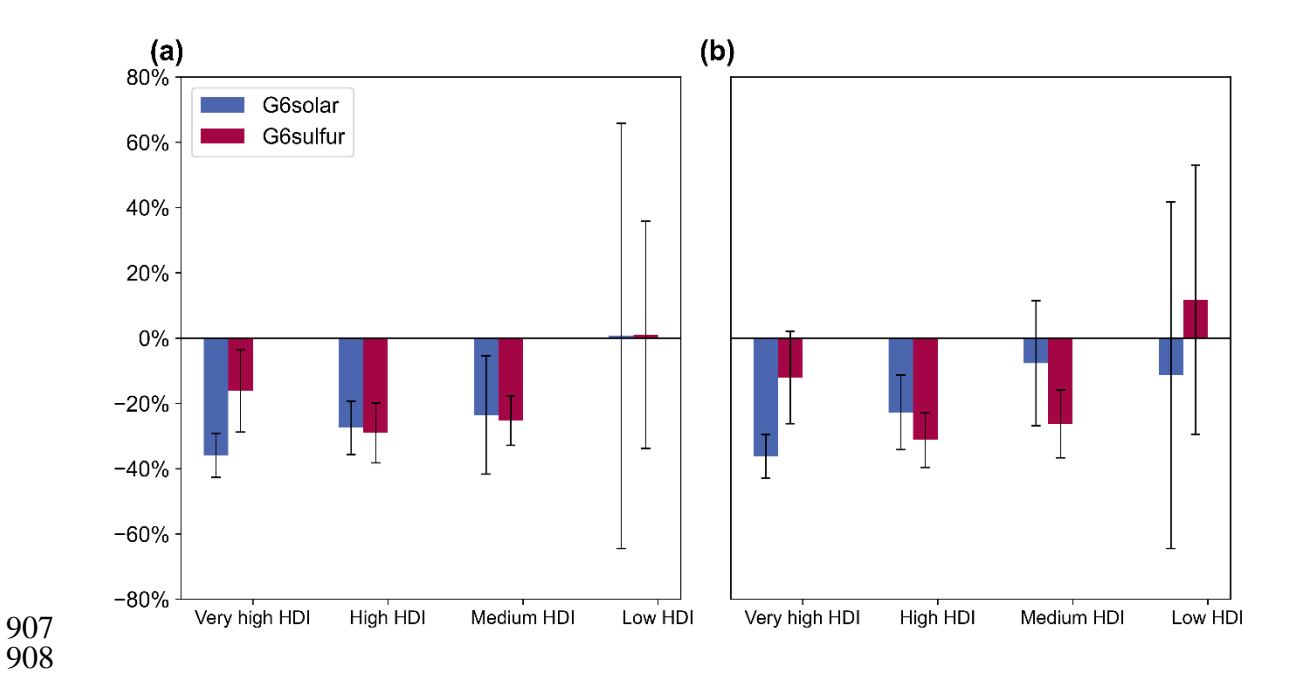


Figure 12. The same as Figure 8 but present-day GDP and population is applied.



**Figure 13.** The same as Figure 10 but present-day GDP and population is applied.

**Table 1**. Summary of the GeoMIP6 models used in drought assessment.

Models	Stratospheric aerosols in G6sulfur	Resolution
CNRM-ESM2-1	Prescribed aerosol distribution	1.4°×1.4°
IPSL-CM6A-LR	Actual SO <sub>2</sub> injections	2.5°×1.25°
UKESM1-0-LL	Actual SO <sub>2</sub> injections	1.875°×1.25°
MPI-ESM1-2-HR	Prescribed aerosol distribution	0.9375 °× 0.9375°
MPI-ESM1-2-LR	Prescribed aerosol distribution	1.875° × 1.875°

**Table 2.** Summary of the GLENS experiment used in drought assessment.

Experiment	Model	Time Series	Members
Control	CESM1(WACCM)	2010-2097	3
Control	CESM1(WACCM)	2010-2030	17
Feedback	CESM1(WACCM)	2020-2099	20

**Table 3**. Summary of scPDSI calculated with varied meteorological forcings.

Name	Temperature	Precipitation	Radiation	Period
HIST	HIST	HIST	HIST	1995-2014
SSP585	SSP585	SSP585	SSP585	2081-2100
G6sulfur	G6sulfur	G6sulfur	G6sulfur	2081-2100
G6solar	G6solar	G6solar	G6solar	2081-2100
$T_{G6sulfur}P_{S5}R_{S5}$	G6sulfur	SSP585	SSP585	2081-2100
$T_{S5}P_{G6sulfur}\:R_{S5}$	SSP585	G6sulfur	SSP585	2081-2100
$T_{S5}P_{S5}\;R_{G6sulfur}$	SSP585	SSP585	G6sulfur	2081-2100
$T_{G6solar}P_{S5}R_{S5}$	G6solar	SSP585	SSP585	2081-2100
$T_{S5}P_{G6solar}\ R_{S5}$	SSP585	G6solar	SSP585	2081-2100
$T_{S5}P_{S5}\;R_{G6solar}$	SSP585	SSP585	G6solar	2081-2100
$T_{HIST}P_{S5}\;R_{S5}$	HIST	SSP585	SSP585	2081-2100
$T_{S5}P_{HIST}\;R_{S5}$	SSP585	HIST	SSP585	2081-2100
Ts5Ps5 Rhist	SSP585	SSP585	HIST	2081-2100